LSU Master's Theses   Graduate School

2014

Study of the low energy solar neutrino spectrometer (LENS) concept with the uLENS prototype

Liudmyla Afanasieva
Louisiana State University and Agricultural and Mechanical College

STUDY OF THE LOW ENERGY SOLAR NEUTRINO SPECTROMETER
(LENS) CONCEPT WITH THE μLENS PROTOTYPE

A Thesis

Submitted to the Graduate Faculty of the
Louisiana State University and
Agricultural and Mechanical College
in partial fulfillment of the
requirements for the degree of
Master of Science

in

The Department of Physics and Astronomy

by
Liudmyla Afanasieva
B.S., Kharkiv National University, 2009
May 2014

TABLE OF CONTENTS

ABSTRACT

Neutrinos are a useful tool that serves as an immediate probe of the Sun's core providing insight into the details of the Sun's energy production, internal composition and structure. Across the globe a number of solar neutrinos experiments have helped to clarify various characteristics of the solar neutrino spectrum. However, little experimental information is known regarding low-energy solar neutrinos, which comprise about 90% of the total solar neutrino spectrum. With this in mind, we are developing the Low Energy Solar Neutrino Spectrometer (LENS), an indium-based liquid scintillator detector with the capability to precisely measure the full spectrum of solar neutrinos, including pp, ^{7}Be, pep, and CNO neutrinos, through the charged current reaction.

Due to the high sensitivity required to detect low energy neutrinos, the LENS concept must aim for precise time and spatial correlations. This is to be accomplished using a highly segmented optical lattice architecture, where total internal reflection of light produces excellent spatial resolution. A program of R&D is being conducted to test the future performance of the LENS detector technology. This thesis focuses on construction and testing of the first prototype, μ LENS, a small-scale detector prototype with 110 liters of Linear alkylbenzene (LAB) scintillator designed to test construction techniques and light transport in the scintillation lattice architecture.

A number of measurements with the μLENS prototype were performed. We studied light channeling inside the detector by illuminating it with external radioactive sources. The patterns of light reaching the outer surface of the μ LENS were measured with an array of photomultipliers. A data acquisition system and analysis codes were developed to collect and process the data. The γ background rates inside the Kimballton Underground Research Facility (KURF) were also studied using a NaI detector and the μLENS prototype. We also performed a

test of light transport with external LEDs. The next step in the development of LENS is construction of miniLENS, a next generation prototype detector that will include external shielding to probe the absolute sensitivity of the LENS concept at neutrino rates.

CHAPTER 1. INTRODUCTION

The Standard Solar Model developed by John Bahcall and colleagues is based on the concept that solar energy is the product of nuclear reactions that convert hydrogen in the Sun into helium [1,2]. Hydrogen is the most abundant element in the Universe, and the fusion of four protons into an α particle, positrons, and neutrinos, provides a release of about 27 MeV of thermal energy [2]. About 600 million tons of hydrogen must be burned every second to supply the solar luminosity. A question that arises is what are the details of how this fusion process takes place.

Estimates show that the probability for the simultaneous interaction of four protons in the stellar plasma is far too small to account for the observed luminosity of stars. Instead, sequences of interactions involving two particles in the entrance channel are much more likely to occur. The two predominant ways by which hydrogen is converted to helium in hydrostatic hydrogen burning are the proton–proton (or pp) chains and the carbon-nitrogen-oxygen (CNO) cycles. These processes were first suggested more than 60 years ago [3]. Nuclear physicists have worked for half a century to determine the details of the nuclear reactions involved in these processes. The details of the nuclear processes depend sensitively on the temperature [4]. In stars with masses below $M \approx 1.5 \, M_\odot$, hydrogen fusion proceeds predominantly via the pp chains while more massive stars burn hydrogen via the CNO cycles, which are illustrated in Figure 1. The thermal energy that is supplied by nuclear fusion ultimately emerges from the photosphere of the Sun, but it takes more than 10^5 years for the energy produced in the Sun's core to diffuse to the surface as the mean free path for photons in the dense inner radiative zone of the Sun is only about 1 mm. The photospheric luminosity of the Sun is thus largely decoupled from the energy source in its core [5].

As part of the nuclear energy generation processes in the core of the Sun, electron-flavor neutrinos are produced from weak interactions. The neutrino has a less tortuous path out of the Sun's core since the neutrino rarely interacts with ordinary matter. Neutrinos travel from the core of the Sun to its surface at nearly the speed of light, and then take less than 8.5 minutes to travel the distance from the Sun to the Earth. The Sun is an abundant source of neutrinos, with approximately a hundred billion solar neutrinos crossing every square centimeter on Earth every second. The detection of solar neutrinos provides an opportunity to directly probe the nuclear processes in the Sun's core, telling us about the conditions in the Sun's core as it was only 8.5 minutes ago and providing insight into the nuclear processes that fuel our Sun.
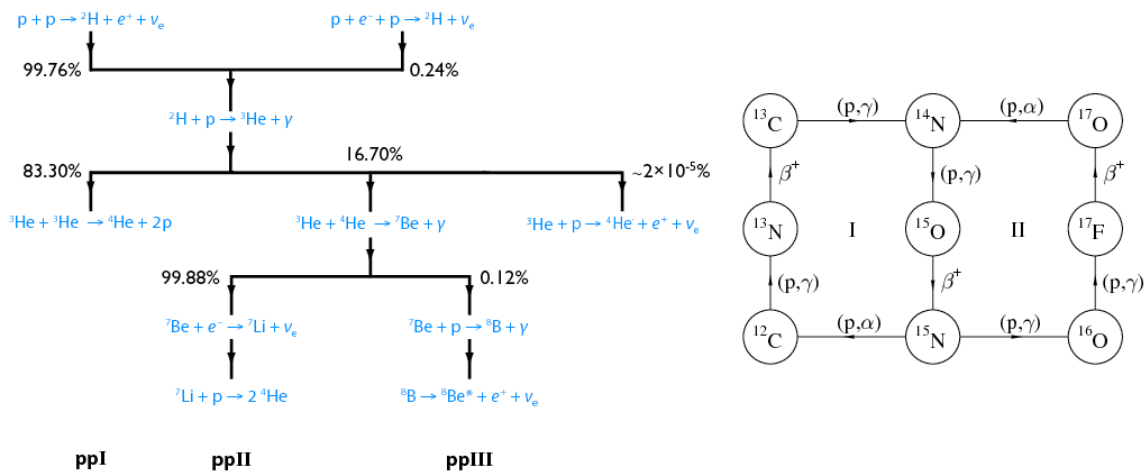
Figure 1. Mechanisms for energy production in the Sun via the pp chains and Carbon-Nitrogen-Oxygen cycles. Reproduced from [6].

Of the fundamental reactions in the solar energy-generating process, the ^{1}H(p,d) reaction (pp) produces the great majority of solar neutrinos, see Figure 1 [6]. The nuclear reactions that involve isotopes of carbon, nitrogen, and oxygen, known as the CNO reactions, contribute only about 1% of the solar luminosity and relatively small neutrino fluxes. Several other reactions produce neutrinos with a continuum of energies. The ^{7}Be electron capture, however, takes the ^{7}Li

nucleus into one of two states producing monoenergetic neutrinos with neutrino "line" emission at one of two energies. Similarly, the pep reaction produces a neutrino emission line. The rate of these reactions (and the distribution of neutrino energies) depends on the detailed model used for the Sun. The complete spectrum of solar neutrinos as predicted by the Standard Solar Model is shown in Figure 2.

Solar neutrino experiments are providing keen insight into fusion in the Sun's core. Different experimental techniques provide sensitivities that vary with the neutrino energy. The first experiments such as SAGE, GALLEX, and HOMESTAKE used radiochemistry to detect a total integrated neutrino flux over at broad range of energies. In these experiments only the number of neutrinos could be measured, but not their incident energy spectrum. These experiments were the first to report a "neutrino problem" when every radiochemical experiment measured a shortfall of neutrinos. About one to two thirds of the neutrinos expected were observed in each case. In the case of GALLEX, 80 neutrino events were measured where 120 were expected, and the discrepancy was about two standard deviations, which was the best result at that time. The possible explanations that were considered to explain the shortfall either focused on problems with the solar model or that something that happens to the neutrinos during their flight over the 150 million km journey to Earth [7,8,9,10].

Other experiments used water Cerenkov detectors such as Kamiokande, and Super-Kamiokande (SK) to detect high-energy neutrinos in real-time. The disadvantage of such detectors is the low luminosity of light from the Cerenkov effect resulting in a high threshold energy for electrons required to produce measurable Cerenkov light above backgrounds. Thus, they are limited to only the highest energy neutrinos, which have a relatively low flux requiring enormous detector masses to achieve good statistics. Borexino, a liquid scintillator based

detector, now has pushed the energy threshold for real time detection of solar neutrinos to energies as low as about 0.6 MeV, low enough to accurately measure the flux of the ^{7}Be solar neutrino flux. In the next section we briefly summarize progress in such spectroscopic solar neutrino experiments and the scientific impact.
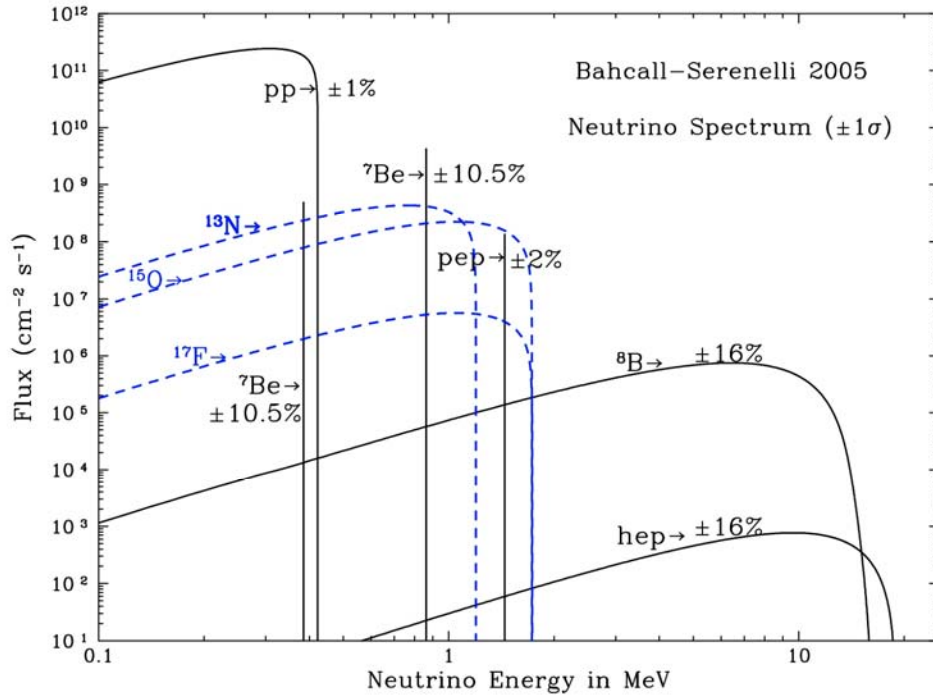
Figure 2. Expected solar neutrino spectrum from the standard solar model reproduced from [11].

These experiments observed a deficit of neutrinos via charged current reactions compared to the SSM (the solar neutrino problem), but they also provided the resolution to this problem, conclusive evidence for neutrino oscillations and physics beyond the standard model of particle physics. In Chapter 3 we will provide an overview of the LENS concept for a next-generation neutrino detector. In Chapter 4 and 5 we describe development of the first prototype, and we discuss the measurements that were performed with the prototype in Chapter 6. Plans for the future involving a larger prototype are then summarized in Chapter 7.

CHAPTER 2. SOLAR NEUTRINO DETECTORS OVERVIEW

2.1. Super-Kamiokande (SK)

The Kamiokande detector (for the Kamioka Nucleon Decay Experiment) was a tank containing 3,000 tons of pure water with about 1,000 photomultiplier tubes (PMTs) attached to the inner surface. Construction of Kamiokande was completed in April 1983, and the experimental aim was to detect proton decay, one of the fundamental questions of elementary particle physics. The size of the tank was 16.0 m in height and 15.6 m in diameter. An upgrade of the detector was started in 1985 to observe neutrinos of cosmic origin via neutrino-electron elastic scattering:

$$\nu_x + e^- \rightarrow \nu_x + e^- \tag{1}$$

where ν_x is a neutrino of either electron, mu or tau flavor. The detector was highly sensitive and succeeded in detecting neutrinos from supernova 1987a, which was observed in the Large Magellanic Cloud in February 1987. Solar neutrinos were observed in 1988, confirming the deficit of neutrinos from SSM predictions observed by the Homestake experiment [12].

Despite its success in neutrino observation, Kamiokande could not detect proton decay, its primary aim. Higher sensitivity was also needed for neutrino observations. This led to the construction of Super-Kamiokande (SK), with ten times more water volume and PMTs than Kamiokande. SK started operations in 1996. The SK Collaboration announced the first evidence of neutrino oscillations in 1998 from observations of atmospheric neutrinos [13] building strong evidence that neutrinos have non-zero mass. Until this, all observational evidence was consistent with neutrinos being massless, although theorists had speculated on the possibility of neutrinos having non-zero mass for many years. However, if neutrinos are massive, the states of definite flavor may not coincide with states of definite mass, and then, neutrinos are produced in a

superposition of different mass eigenstates. As neutrinos propagate, their eigenfunction evolves so that the probability of finding different flavor eigenstates varies with distance, hence we say that neutrinos "oscillate", a phenomenon first pointed out by B. Pontecorvo [14,15].

Since SK operates by detection of Cherenkov light in water, it can only observe the high-energy [8]B neutrinos and hep neutrinos originating from the [3]He + p reaction. However, the direction and energy of the recoiling electrons are reconstructed from the Cherenkov cone, so neutrino interactions are recorded in real-time and point back to the sun. Also, the large fiducial mass of the innermost 22.5 kton of the detector results in a large solar neutrino interaction rate of about 15 events/day above 5 MeV after event selection. Since SK is doing measurements in real time, day-night and seasonal effects of the solar neutrino flux can also be measured. The other advantage of this method is the measurement of the recoil electron energy that allows the solar neutrino spectrum to be measured.

Oscillations of solar neutrinos have been studied in numerous data runs with SK. The results from each run have placed increasingly stringent constraints on the mixing angle between neutrino mass and flavor eigenstates, as well as on the neutrino mass difference. The combined results of the SK runs are that the [8]B solar neutrino flux was measured to be $\Phi = 2.31 \pm 0.02_{(stat)} x 10^6/cm^2 s$.

The solar neutrino oscillation parameters predict a fairly small day/night asymmetry (about 1.5%). To eventually measure such a small asymmetry requires excellent control of systematic effects and a very large data sample. The well-calibrated SK detector with its large fiducial mass of 22.5 kton is at present the only detector that can probe such small asymmetries. Using calibration data taken with a deuterium-tritium (DT) neutron generator (which produces [16]N in situ via a charge-exchange reaction with ^{16}O) [16] this systematic effect can be verified.

2.2. The Sudbury Neutrino Observatory (SNO)

The Sudbury Neutrino Observatory (SNO) was a water Cherenkov detector for ^{8}B solar neutrinos located 2 km underground in INCO Ltd.'s Creighton nickel mine near Sudbury, Ontario [17]. The SNO detector, unlike previous detectors, used heavy water to be sensitive to three reactions with one of them fully sensitive to all neutrino flavors that would allow a direct test of neutrino oscillations. All of the solar neutrino detectors prior to SNO had been sensitive primarily or exclusively to electron neutrinos and yielded little information on muon neutrinos and tau neutrinos. The Creighton Mine in Sudbury, among the deepest in the world was an ideal place for SNO due to the high suppression of cosmic rays by the tremendous (2092 meters) rock overburden, which is 5890 meters water equivalent. The detector operated from May 1999 until November 2006.

SNO's central target volume consisted of 1000 tons of ultra-pure heavy water (D_2O) contained in a 12 m diameter acrylic vessel. The heavy water was viewed by an array of ~9500 inward-looking photomultiplier tubes arranged on a 17.8 m diameter geodesic sphere. The region between the photomultipliers and the acrylic vessel contained ultra-pure light water for shielding. The heavy water target allowed SNO to detect solar neutrinos through three separate interactions, the charged current (CC) reaction, the elastic scattering (ES) reaction, and the neutral current reaction:

$$\nu_e + d \rightarrow p + p + e^- \ (CC) \tag{2}$$

$$\nu_x + e^- \rightarrow \nu_x + e^- \ (ES) \tag{3}$$

$$\nu_x + d \rightarrow p + n + \nu_x \ (NC) \tag{4}$$

The charged current (CC) reaction is exclusively sensitive to the electron neutrinos, ν_e's, and so measures the total flux of the electron neutrinos. The kinetic energy of the electron can be

correlated with the initial neutrino energy, allowing the energy spectrum of the ν_e's to be measured. The Q value for the CC reaction on deuterium is -1.4 MeV. The direction of the relativistic electron produced in the CC reaction is weakly anticorrelated with the incoming neutrino's direction. For solar neutrinos, the angular distribution of the CC reaction is approximately $1 - (1/3)\cos\theta_\odot^2$ [18], where $\theta_\odot$ is a mixing angle responsible for the solar ν_e neutrino oscillations.

By itself, the elastic scattering (ES) reaction cannot provide a measure of the total [8]B neutrino flux or its flavor content. Comparison of the [8]B flux deduced from the ES reaction, assuming no neutrino oscillations [$\phi^{ES}(\nu_x)$], to that measured by the CC reaction [$\phi^{CC}(\nu_x)$],] can provide clear evidence of flavor transformation without reference to solar model flux calculations. If neutrinos from the Sun change into other active flavors, then $\phi^{ES}(\nu_x) < \phi^{CC}(\nu_x)$ [19].

Sensitivity to the ES reaction, which was also the basis for neutrino detection by SK, occurs for all active neutrino flavors, but the cross-section for scattering by ν_e's is 6.5 times larger than the cross-section for ν_μ or ν_τ. The rate of elastic scattering interactions is thus proportional to $\phi(\nu_e) + 0.514\left(\phi(\nu_\mu) + \phi(\nu_\tau)\right)$[19]. The direction of the scattered electron is strongly correlated with the initial neutrino's direction. This strong directionality makes it easy to distinguish the ES signal from other neutrino signals or the background noise. The energy of the scattered electron is weakly correlated with the initial neutrino's energy.

Sensitivity to the neutral current (NC) reaction was the unique feature of SNO; it occurs for all active neutrino flavors with equal probability. SNO measured NC interactions by observing the neutrons liberated by this reaction. In pure D₂O, approximately 30% of these neutrons capture on a deuteron, emitting a 6.25 MeV γ-ray. This γ-ray Compton scatters, and SNO then

detects the resulting Compton electron. The neutral current reaction provides no directional information about the interacting neutrinos, and simply measures the total neutrino rate above its threshold energy of 2.2 MeV.

By measuring solar neutrinos with these interactions, SNO directly probed for neutrino flavor conversion. If ν_e's are being converted into ν_μ or ν_τ, the [8]B flux inferred from the NC or ES interactions, which each have sensitivity to all neutrino flavors, will exceed the rate inferred from the CC interaction, which measures only ν_e's.

The establishment of SNO [17,18] motivated an intensive theoretical effort to make reliable estimates of the neutrino-deuteron reaction cross-sections [19,20,21]. SNO published the first results for the CC and ES fluxes in June 2001. This data set consisted of 240.95 live-days, and spanned the period from 2 Nov 1999 to 15 Jan 2001 [19]. The first report from SNO [18] shows a strong evidence for ν_e oscillations by combining the SNO data on the charged-current (CC) reaction with the Super-Kamiokande data on neutrino-electron elastic scattering (ES) [22]. The accuracy of this important conclusion depends on the precision of theoretical estimates for the νd -reaction cross sections. Thus, SNO observed NC fluxes consistent with the SSM, providing conclusive evidence for neutrino oscillations.

2.3. Borexino

Borexino is a 100 t fiducial volume organic liquid-scintillator detector. The primary aim of the experiment was to make a precise measurement of the [7]Be neutrino flux from the Sun and compare it to the Standard Solar Model prediction. This allows scientists to further understand the nuclear fusion processes taking place at the core of the Sun and also helps to determine properties of neutrino oscillations, including the Mikheyev–Smirnov–Wolfenstein (MSW) effect, a particle physics process that modifies neutrino oscillations in matter. Detection of the

monoenergetic [7]Be neutrinos is particularly interesting since they fall in an energy regime near the transition between MSW dominated and vacuum dominated oscillations and can be used to constrain extensions to the standard model of particle physics. Other goals of Borexino are to detect [8]B, pp, pep and CNO solar neutrinos as well as antineutrinos from the Earth and nuclear power plants. Borexino could also detect neutrinos from a supernova within our galaxy [23].

Borexino has high radiopurity requirements to achieve detection of such low energy neutrinos. With a necessary radioactivity equivalent of less than 10^{-9} Bq/kg, the core of Borexino had to be 9-10 orders of magnitude less radioactive than any naturally occurring material on Earth. A one ton fiducial mass prototype, the Counting Test Facility (CTF), demonstrated the feasibility of large scale purification of organic liquid scintillators to the levels required for [7]Be neutrino detection. After successful demonstration of the purification techniques, the construction of Borexino occurred between 1998 and 2007 in the Laboratori Nazionali del Gran Sasso (LNGS), located in the central Apennine Mountains at approximately 100 miles north-east of Rome, Italy. The underground portion of the laboratory is covered by rock of about 1400 m with a shielding capacity against cosmic rays of 3800 meters water equivalent (m.w.e.).

Employing the liquid-scintillator technology at record high radiopurity levels, Borexino was the first experiment to directly measure the solar neutrino spectrum below 3.5 MeV [24,25,26]. The experiment was commissioned in May 2007 and has been taking data ever since. To this moment, Borexino is still the only operating detector with the sensitivity to such low energy neutrinos.

Borexino uses elastic scattering similar to SNO and SK, but in Borexino the scattered electron deposits its energy in the scintillator, producing much higher light output, which is detected by an array of photomultiplier tubes (PMTs). With a mean free path of at most a few

centimeters in scintillator, the recoil electron is an almost point like light source and provides no directional information on the original neutrino. Moreover, β- and γ-emission from radioactive background produce signals that are indistinguishable from ν-signals on an event-by-event basis. Thus, the ultra-high level of radiopurity required.

Borexino accomplished the first real-time detection and precision measurement of neutrinos from ^{7}Be electron capture. The monoenergetic 862-keV solar neutrinos from electrons captured by ^{7}Be provide a distinctive Compton-like recoil spectrum with a shoulder at 665 keV electron energy. Besides testing the Standard Solar Model, the ^{7}Be neutrino flux provides an excellent probe of the transition from the vacuum-dominated regime of neutrino oscillations according to the MSW matter enhanced oscillations.

In September 2011 Borexino published a precision measurement of the solar ^{7}Be neutrino flux yielding a neutrino-induced electron scattering rate of $\left(46.0 \pm 1.5_{stat}{}^{+1.5}_{-1.6}{}^{syst}\right)(day *$ $100ton)^{-1}$ [27]. Using the neutrino oscillation parameters of [28], this measurement translates to a flux of $\Phi\left(^7\text{Be}\right)(4.84 \pm 0.24) \cdot 10^{-9} cm^{-2} s^{-1}$, corresponding to a ratio of measurement to the SSM expectation of 0.97 ± 0.09 [27].

Alternatively, fixing the ^{7}Be neutrino flux according to the SSM expectation, a ν_e surival probability of $P_{ee} = 0.51 \pm 0.07$ at 862 keV was found. In addition, the absence of a day-night asymmetry in the ^{7}Be-ν interaction rate [29] was reported:

$$A_{dn} = 2\frac{R_N - R_D}{R_N + R_D} = 0.001 \pm 0.012_{stat} \pm 0.007_{syst} \qquad (5)$$

where R_N and R_D denote the ^{7}Be flux rate at night and at day, respectively. The result is compatible with zero and in agreement with the prediction of the MSW-LMA solution. Borexino has also reported the first evidence of pep neutrinos combined with an upper limit on the CNO-ν flux. The respective scientific achievements are described in detail in [24,25,28,27,30].

CHAPTER 3. LENS CONCEPT AND MOTIVATION

Despite the experiments conducted thus far, there is little experimental information regarding low-energy solar neutrinos, which comprise about 90% of the total solar neutrino spectrum. The only information on the flux of neutrinos from pp fusion that provides the bulk of energy generated in the Sun comes from integral radiochemical experiments. The low-energy solar ν spectrum (<2 MeV) offers a palette of fluxes at energies ideal for probing flavor physics via the energy dependence of ν-flavor survival and unique access to direct experimental proof for the still incomplete MSW-LMA ν-flavor conversion model, for new scenarios of non-standard particle physics, and an overall precision test of ν physics and astrophysics using the fundamental equality of the ν-derived solar luminosity L_ν to the precisely known photon derived luminosity of the Sun $L_\odot$ [31]. Any inequality $L_\nu / L_\odot \neq 1.00$ that survives at high precision has great implications. This objective requires the measurement of not only pp ν's but the complete set of pp, ^{7}Be, pep, & CNO ν fluxes (which together make up > 99.99% of the ν luminosity) clearly resolved into individual fluxes with minimal background uncertainty. Energy-specific charged-current (CC)-based ν detection is essential for this purpose. This is the mission of LENS.

The luminosity balance $L_\nu = L_\odot$ is based on broad astrophysical assumptions. First, nuclear reactions are the sole source of energy in the Sun. Second, the Sun is in a quasi-steady state of energy generation. The energy observed at present originated more than 10^5 years ago, while ν signals are indicative of the energy generated in the Sun now. If eventually, with our best knowledge of ν's, an inequality is revealed, major new science is exposed: $L(\nu) > L(\gamma)$ would imply that the Sun may be getting hotter with time; while, $L(\nu)<L(\gamma)$ could imply cooling or signal the discovery of a non-nuclear source of the Sun's energy (or of sterile neutrinos). A

global analysis of the LENS results for the different fluxes provides an independent precision measurement of neutrino parameters such as θ_{12}, now that θ_{13} has been measured [34,35].

The unconverted ν_e fluxes at the Sun can be deduced from the complete low-energy ν_e flux measured by LENS assuming our current published understanding of the ν_e survival probability, $P_{ee,}$ is correct. Each of the low-energy ν fluxes in turn implies a known energy release through a specific reaction chain in the Sun [31]. Thus the total energy released from the Sun's core can be determined – the solar luminosity inferred via ν's: L_ν.

Since LENS determines P_{ee} for the broadest range of energies of any single experiment, analysis of the transition region between vacuum- and matter-dominated oscillation regimes can be directly and self-consistently probed to reveal deviations that would indicate fundamentally new particle physics (e.g. non-standard weak interactions) [36,37,38]. Further, all particle physics information is obtained using neutrinos exclusively so that a comparison with reactor neutrino results [34,35,39] (which used antineutrinos) will set limits on possible violation of the CPT symmetry in the neutrino sector.

Measurements of the CNO ν flux are also of fundamental importance for reconciling the lower observed abundances of heavier elements in the Sun's atmosphere that result in a direct conflict with helioseismology and our understanding of size of the Sun's convective zone. This discrepancy calls into question the basic assumption of a homogenous Sun. Measurement of the CNO solar neutrino flux is the only way to directly probe the abundance of these elements in the Sun's core. The signal/background specificity in LENS for the CNO measurement is especially attractive in comparison to other approaches that depend on the ν-electron scattering process that is not energy specific. The potential for discovering new physics/astrophysics via low-energy ν's and the emergence of the required new technology are timely. The first real-time spectroscopy of

[7]Be solar ν's by Borexino is a breakthrough that provides fresh impetus to the program of low-energy ν research. In particular, the CC+NC-based Borexino result offers a key complement to the CC-based LENS detector (similar to the situation with SK and SNO). With these developments, solar-ν research is far from "mined out"; indeed, LENS is set to chart new directions in precision spectroscopy for astrophysics and ν physics. For the first time, the needed technology to accomplish these important scientific goals is available in (and only in) LENS.

Predictions of the Standard Solar Model have so far provided the fundamental basis for interpreting and evaluating measured solar neutrino fluxes. The latter have verified the basic assumptions that lead to the conclusion that the dominant energy mechanism in the Sun is the proton-proton (pp) chain with a significantly smaller contribution due to the CNO cycle of reactions. The basic confirmation of the SSM comes not only from ν results but also agreement with results from helioseismology. However, in recent years, the good agreement of the Standard Solar Model (SSM) with helioseismology has come into question, and the focus has turned to measurement of the CNO neutrino fluxes as a way to shed further light on this issue.

The solar model flux predictions depend fundamentally on the metallicity in the Sun – particularly the abundances of the light elements C, N, O. In the past decade, more sophisticated three-dimensional models of the solar atmosphere have been developed, significantly improving the agreement between predicted and observed absorption line shapes [40, 41], but also yielding a photospheric metal abundance ~30% below previous one-dimensional model values [42]. The resulting lower metallicity has the effect of destroying the agreement with helioseismic measurements of the speed of sound in the Sun, as seen in Figure 3 [43]. The ν fluxes are also affected (see Figure 4), with the CNO fluxes being the most strongly affected [43]. The CNO
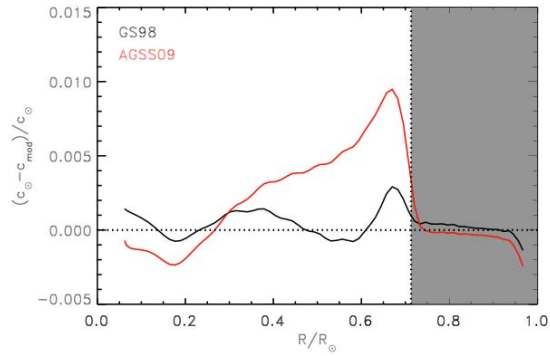
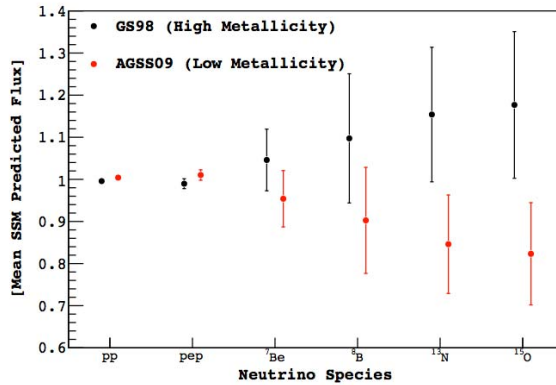Figure 3. Relative comparison of sound speed from SSM to helioseismological observations [38].

Figure 4. Comparison of predicted solar neutrino fluxes under two abundance assumptions [40].

problem is much more than the local conflict of ν fluxes: the understanding of CNO reactions reaches well into the general problem of star formation and the place of solar evolution in this framework [44].

Thus we have a new problem, one that calls into question the fundamental assumption of a homogeneous sun. A measurement of the CNO neutrino flux would provide the only probe of the CNO abundance in the interior of the Sun to potentially resolve this conflict, but to date there are only upper limits from solar neutrino experiments [45]. This requires massive scintillation detectors such as Borexino and the future SNO+ [46] that are sensitive to low energies. However, these detectors, based on e $-\nu$ scattering yield untagged electron recoil continua that

are frequently indistinguishable from background, particularly from impurities such as [210]Bi even in the extremely small concentrations achieved in Borexino. Cosmic ray secondaries such as ^{11}C are a further serious problem, though less so in SNO+ because of its deep location. It is here that LENS can play a decisive role. LENS ν detection has a distinct signature, which discriminates against such backgrounds. The CC-based method gives the CNO spectrum directly (unlike electron recoil, which smears at the incident ν spectrum) that can be clearly resolved (as seen in Figure 4) from the line features due to other low-energy solar ν features. Tagging on the γ-cascade in LENS provides a background-free measurement for CNO neutrinos, unlike for elastic scattering experiments, and one can actually distinguish neutrinos from ^{13}N from [15]O decay. This is unique to LENS.

Neutrino detection in LENS is based on the CC *tagged* ν_e reaction on [115]In [32]:

$$\nu_e + {}^{115}In \rightarrow e^- + (\tau = 4.76\ \mu s)\ 2\ \gamma\ +\ {}^{115}Sn \qquad (6)$$
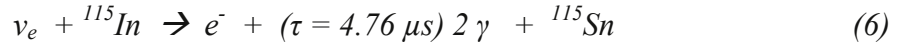
The detection medium is an organic liquid scintillator containing 6-8 % by weight of indium (In-LS). The reaction provides a prompt e⁻ signal that uniquely specifies the incident ν energy. The Q value is only 114 keV [33], the lowest known for CC neutrino capture, providing sensitivity to >95% of the pp ν continuum (0-420 keV). The prompt electron is followed by a tag of 2 γ's after a mean delay of $\tau = 4.76$ μs, as illustrated in Figure 5. This tag is the central feature that allows neutrino-induced events to be cleanly separated from background. Finally, the natural abundance of [115]In is ~96%, so a high fractional target mass can be achieved without isotopic enrichment.

For the pp neutrinos, however, a major background arises from the natural β-activity of [115]In that produces ~10^{11} β's per pp solar neutrino charged-current event, Figure 6. Precise time and spatial correlations between the prompt electron and the delayed gamma cascade are required to suppress this background. In practice, the space- and time-delayed coincidence of the

In ν tag in LENS reduces this ratio to a more tractable ~10^5. The signal in LENS is a delayed coincidence event. Thus, internal contamination (such as ^{14}C), with a specific activity far less than that of In β-decay, is not an issue in LENS. Random external γ's together with In events can mimic the tag but they are controllable by passive shielding and a fiducial volume cut. Although cosmogenic secondary protons can produce the same tag cascade as the ν signal, their rate is adequately low at a depth of 2000 mwe and they can be efficiently identified (via neutron capture).
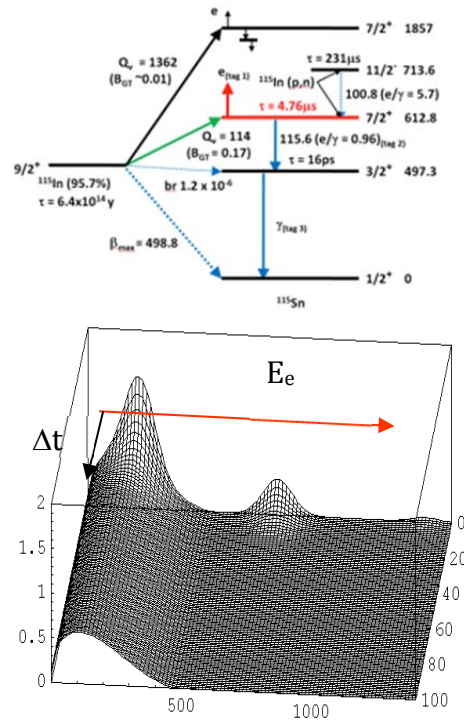

Figure 5. (top) Level scheme of ^{115}Sn, showing the prompt beta (tag 1), followed by the delayed cascade (tag 2) and (tag 3). The time between this 'start' and 'stop tag' provides Δt, which is then graphed versus the energy of the prompt beta (bottom). At each energy, a fit to a decaying exponential plus constant background provides the neutrino flux at that energy (plus Q-value).
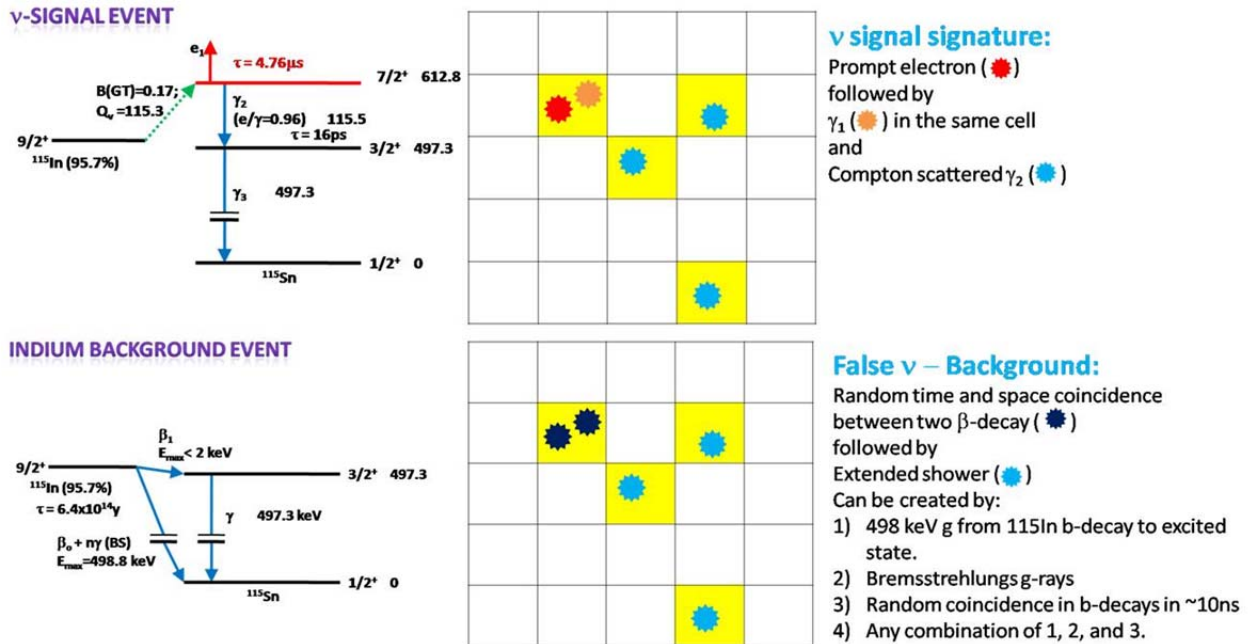
17

Figure 6. The "useful" event resulting from neutrino interaction with In (top) and the "false" signal, which comes from In decays and can look as our "useful" signal (bottom). In case of the "useful" event a prompt electron (red) is emitted, followed by the gamma cascade (orange), which deposits light (blue) 2-3 cells from the cell where the event occurred. The indium background event results from random time and space coincidence between different In decays. Two In decay events happen in a call (derk blue) and are followed by the compton showers (blue), which deposit light in the body of the detector.

Precise spatial and digital resolution is achieved by employing an "optical lattice" design as illustrated in the small acrylic air lattice shown in Figure 7. A concept for a full LENS detector layout is shown in Figure 8. Light is channeled via total internal reflection (TIR) along the three axes intersecting the cell where energy was deposited, providing segmentation and efficient light collection. The lattice allows one to examine candidate 'stop tags' in great detail. 'Stop tags' deposit energy in the same cell as the prompt beta, and energy in at least two other cells via Compton scattering, with the total sum energy of 613 keV, mimicking the ^{115}Sn γ cascade.
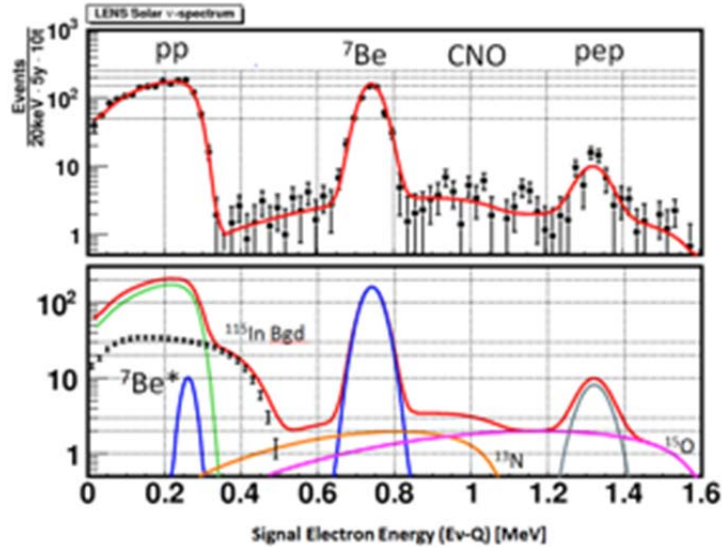
Figure 7. (top) Acrylic/Air Optical Lattice (LENS and miniLENS use a Scintillator/teflon lattice). (bottom) Inset is a cartoon of a 'tagged' neutrino event: the prompt beta (red), followed by a delayed 'tag 2' (peach) – 'tag 3' (blue) cascade. Expected neutrino spectrum from five years of running with 10 tons In.

Background that may cause 'false stop tags' increases the random coincidence rate and is primarily due to: A1) ^{115}In beta decay followed by Bremsstrahlung; A2) ^{115}In beta decay to the 497-keV state of ^{115}Sn (which subsequently gamma decays); B) coincidence between two ^{115}In beta decays, one of which emits Bremsstrahlung radiation; and C) three coincident ^{115}In decays, see Figure 6.

We performed extensive Monte Carlo simulations in attempt to quantify the possible background rates due to the In decay detected parallel to the "useful" neutrino signal during thesame period of time. The simulations showed that the In beta-decay induced 'false tag' rates (in a 5x5x5 fiducial volume of miniLENS per month) result in a signal-to-noise ratio ~ 6 for the pp neutrinos as shown in Table 1.
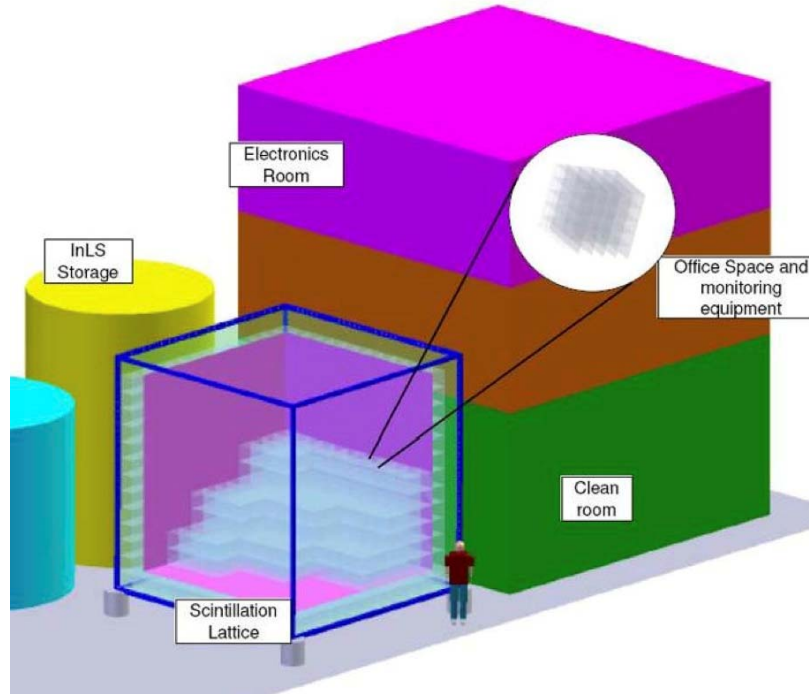

Figure 8. The graphic description of the prospective LENS detector.

Table 1: Computer simulations showing estimated rates of the neutrino-Indium signal and the "false tag" background rates coming from Indium beta-decay.

Rates per month in 5x5x5 cells of mini-LENS	pp Signal	Equiv. Singles	In induced Bgd tot	Bgd A1	Bgd A2	Bgd B	Bgd C
RAW	0.031	265	3.9E+09				
Valid tag (Energy, Branching, Shower) in Space/Time delayed coinc. with prompt event in vertex	0.027	233	5.8E+05	1.8E+05	5.9E+03	4.0E+05	93.0
+ ≥3 Hits in tag shower	0.024	210	1.3E+05	1.2E+05	5.8E+03	3.0E+03	92.6
+Tag Energy = 613 keV	0.022	188	970.5	1.0	11.0	942.9	17.0
+Shower Radius	0.022	186	572.1	1.0	10.8	559.4	1.5
+Hit Separation	0.020	170	28.2	1.0	10.0	17.2	0.008

The false-tag rates due to random coincidences, whether of type B or C, or some other unknown origin, can be studied by artificially widening the cascade time-coincidence window. Cuts on the timing of the neutrino signal and on its spatial signature required the signal should fall within the $10\,\mu s$ window, the deposited light should be detected on average 2-3 cells away from the cell of event, and the light should be deposited in no less than 3 cells simultaneously (7-10 cells on average).

CHAPTER 4. μLENS DETECTOR CONSTRUCTION

In order to determine the performance of the full LENS detector we have been conducting a program of research and development centered around the construction and testing of small detector prototypes. The first prototype built was μLENS. The μLENS detector is a 110 liter prototype instrument that was developed to test construction techniques and light transport in the scintillation lattice architecture in an as-built instrument. μLENS was constructed in a clean room at Virginia Tech University (VT). It consists of a cubic acrylic vessel approximately 0.5mx0.5mx0.5m divided into a lattice, which consists of 6 x 6 x 6 cells constructed from 0.3-mm-thick teflon FEP film supported by 1-mm diameter quartz rods.

Acrylic, quartz and teflon were used since they are stable in organic solvents. Acrylic and quartz also have a comparable index of refraction to the scintillator (Linear alkylbenzene (LAB) in this case), and have a low amount of radioactive contaminants. Also, they are highly transparent making them ideal for this application.

Before the lattice was constructed, all the components of the future detector were precut to high tolerances in a clean room at VT. The lattice structure was constructed first, then the outer acrylic enclosure was assembled around the lattice. The lattice was constructed with horizontal planes of teflon that the quartz rods pass through. Planes of teflon Fluorinated Ethylene Propylene (FEP) were cut as follows: The FEP planes were placed in a template within which receiving holes for quartz rods were punched with a hypodermic needle in a jig that holds the relative hole positions to 0.25 mm tolerance. Then these planes are aligned on pins of another jig, and the final perimeter of the plane was cut.

Next a precision cutting device is used to cut ribbons out of FEP wrapped around a drum as illustrated in Figure 9. Once the teflon was secured on the drum, it was placed on a lathe and

allowed to rotate freely. A custom cutter with two rolling razors spaced 3.25" apart was used to cut uniform 3.25" wide FEP ribbons. These ribbons are then pre-creased using a jig with a hard plastic roller, Figure 10.
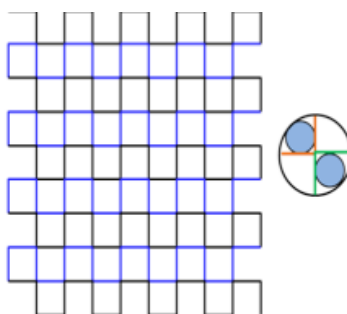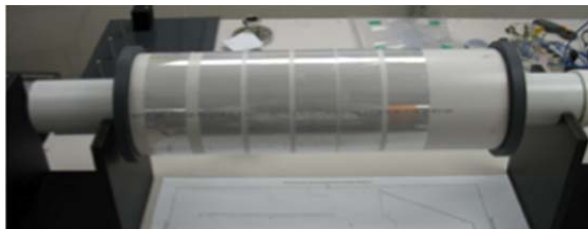

Figure 9. The lathe on which the teflon ribbons were cut (top) and the general structure of the prototype with the quartz rods viewed from the top (bottom). The close-up of two quartz rods in one of the corners of the lattice is shown (bottom).

Holding each end taut, we creased the strip of a ribbon by running a plastic roller along each dull knife-edge of the apparatus. The final crease was then folded and the resulting overlapping sections were sewn together with piano wire. The creases served to allow the teflon strips to properly form the lattice structure. The sewn end fold was used in fastening the strips to their respective quartz rods.

The perimeters of the planes were constructed with tabs that fold down to supply structural support as well as cover the sides of the detector; however, the woven ribbons also cover the sides of half of the outer face as shown in Figure 9. To avoid multiple layers of FEP along the outer edge, large holes were cut in the planes where ribbons cover the edge using a custom built precision hole cutter with the template. The general method applied to build the
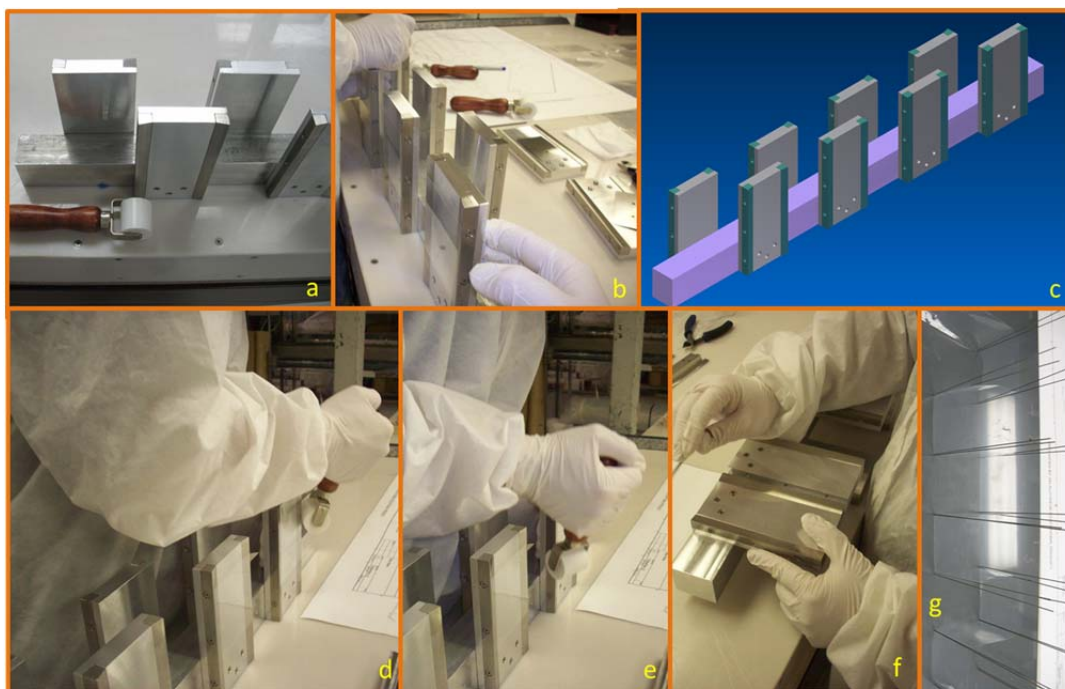
23

Figure 10. Jigs for cutting large planes for the construction of the μLENS lattice.

prototype was to construct the lattice upon the bottom of the outer acrylic vessel without the walls or top for the vessel. The quartz rods inserted into the holes in the acrylic stand vertically and are self-supporting. The planes were constructed near the top of the quartz supports and lowered down onto them. Teflon ribbons were woven around the rods, creating the planes of the detector as shown in Figure 9.

Atop the ribbons, two overlapping half-planes of pre-punched and cut teflon were lowered, thus separating one plane of the detector from another. After the completion of one layer, the layer was lowered slightly, and the new ribbons were woven on top of it. This process was repeated until the lattice was settled at the bottom. The photograph of the nearly completed lattice is shown in Figure 11. Using this technique, the lattice of μLENS was built using thin FEP and quartz rods, minimizing material in the active volume.

Figure 11. The lattice structure for μLENS nearing completion.

To allow for proper placement and sealing of the sides, the vessel walls and bottom have corresponding screw holes. After completing the lattice, we attached the walls to the bottom and inserted some of the screws to hold the structure. Once the walls were secure, the top was carefully lowered into the box. After all the pieces of the acrylic box were assembled, the sides and bottom of the box were sealed together. We loosened the screws and used needles to maintain a small separation between sections while using syringes and wicking to inject acrylic cement. Once the cement covered the appropriate surfaces, the screws were tightened, and the structure was allowed to sit so that proper bonding could occur.

Once completed, the lattice was lowered into an outer wooden supportive structure with holes into which the PMTs would eventually be placed. Finally, the top of the box was tightly screwed on to apply pressure to the top of the vessel. The fully assembled prototype was placed

into a shipping container to transport the detector from the VT campus to Kimballton Underground Research Facility (KURF), including the 3-mile drive over the rocky terrain into the mine. The transportation to KURF was successfully accomplished in fall of 2011 with the only observable damage of 1-2 broken quartz rods. This damage seemed to have no significant effect on the structural integrity of the lattice.

The μLENS prototype at KURF was filled with LAB scintillator (110 liters of LAB with 3g/L PPO and 15mg/L bis-MSB, but with no indium loading) that was prepared at BNL and shipped to KURF for deployment. The production parameters of chemical procurement, purification, and mass-production scheme for LAB-based indium-loaded liquid scintillator were optimized in 2011. A liquid handling system was prepared and installed at KURF for filling, draining and storage of the μLENS prototype. The system includes a 255-L storage PVDF tank, 10-micron filtration system, transfer pumps, associated with all PTFE-based tubing, valves and adapters. Development of liquid handling systems for large prototypes (miniLENS) and the full scale LENS is currently ongoing building upon our experience with μ LENS.

CHAPTER 5. INSTALLING μLENS AT THE KIMBALLTON UNDERGROUND RESEARCH FACILITY

The low-background experimental facility where μLENS is located is at the Kimballton Underground Research Facility (KURF) at Lhoist North America's Kimballton mine in Ripplemead, Virginia. The experimental hall is located on the mine's 14th level at a depth of 1450 m.w.e (meters of water equivalent shielding), and it can be accessed by a vehicle from the surface. The overburden consists of 520 m of dolomite, limestone and other sedimentary rock. Experiments are housed in a 30 m x 11 m laboratory building (shown in Figure 12) that was completed in October 2007. Radon levels in the laboratory have been found to vary from 37 Bq/m^3 in the winter to 122 Bq/m^3 in the summer. Many of the experiments at KURF are housed in separate trailers, but the μLENS prototype is housed in a special dark box container.

Figure 12. Kimballton Underground Research Facility, view of the interior.

5.1. KURF background analysis

Studies of external backgrounds with μLENS are important to understand shielding requirements for a next generation prototype that will directly demonstrate the background levels necessary for the full-scale experiment. Understanding the background environment is also important for assessing the performance of μLENS. We first studied the natural background rates

in the μLENS location using a 5"x5" NaI detector (unshielded). The energy spectrum for the NaI(Tl) was calibrated using ^{137}Cs and ^{60}Co calibration γ-sources.

The efficiency of the NaI was measured with calibrated sources and validated with Monte Carlo simulations. An energy spectrum taken with the NaI is shown in Figure 13. We take the peak observed at 0.6 MeV to be representative of the 0.609 MeV line from [214]Bi decay in the U decay chain (45% branching ratio), the peak at 1.46 MeV to be [40]K (100% branching ratio), and we take the peak at 2.6 MeV to be representative of 2.62 MeV line from the decay of [208]Tl in the thorium decay chain (36% branching ratio). This is summarized in Table 2.

Table 2. Background rate at KURF resulting from the decays of U, K and Th chains.

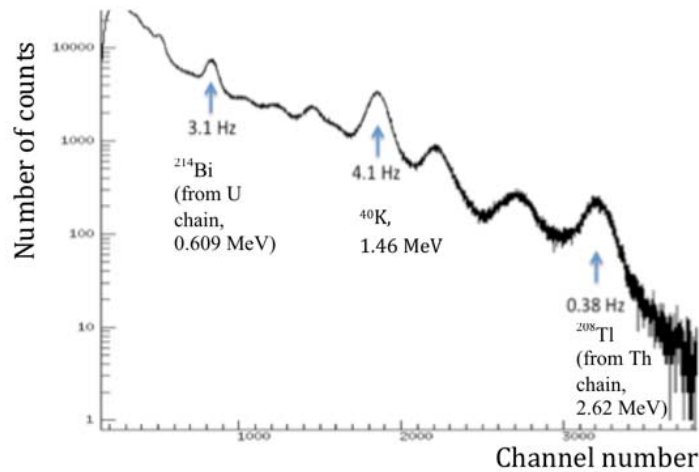| Isotope	-ray energy, MeV	Rate (Hz)	NaI effic.	-branch	-decays/cm²/min
U	0.609	3.1	0.6	0.45	4.3
K	1.46	4.1	0.4	1.0	3.8
Th	2.6	0.38	0.28	0.36	1.4

Figure 13. The KURF background spectrum measured with a NaI detector. Spectra from in the U decay chain, [40]K and Th are seen (from left to right).

28

Some neighboring lines are not resolved due to the relatively poor resolution of the NaI, but the 609 keV U and 2.6 MeV Th lines should be the dominant lines in their respective energy regimes. The rates we derive for the U and Th backgrounds are on the conservative side but reasonable. We were able to measure U, Th and K background rates derived from the yields measured at KURF. We find background levels for U and Th to be about half that measured at LNGS despite our conservative estimates, though the K background is about 50% higher. We also conducted measurements with passive (lead) shielding on some sides to study the directional dependence of the background. We observed no deviation from an isotropic distribution for the U and Th decays, but find that the ^{40}K background has a greater flux from the floor, likely resulting from the concrete floor of KURF. This increased ^{40}K flux from the floor may also explain (at least in part) the larger ^{40}K background in KURF compared to LNGS.

5.2. Dark Containment (DC)

The dark containment for μLENS was designed to be cost effective and light for ease of handling at KURF. The basic design is a stainless steel (SS) 5-sided box with an open top and a channel (Figure 14 and 15) that receives and seals against a 5-sided top box made from aluminized foam sheeting and laminated such that there are no seams with an unblocked path from the outside of the box to the inside. This is shown in Figure 14 and Figure 16.
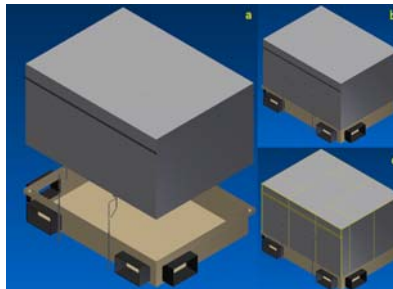

Figure 14. Design of the Dark Containment for μLENS. a) The stainless steel base with cable feed through ports and an elevated foam laminated top on support stilts. b) The top lowered into operation position. c) The seams of outer most shell of the foam laminated top box.

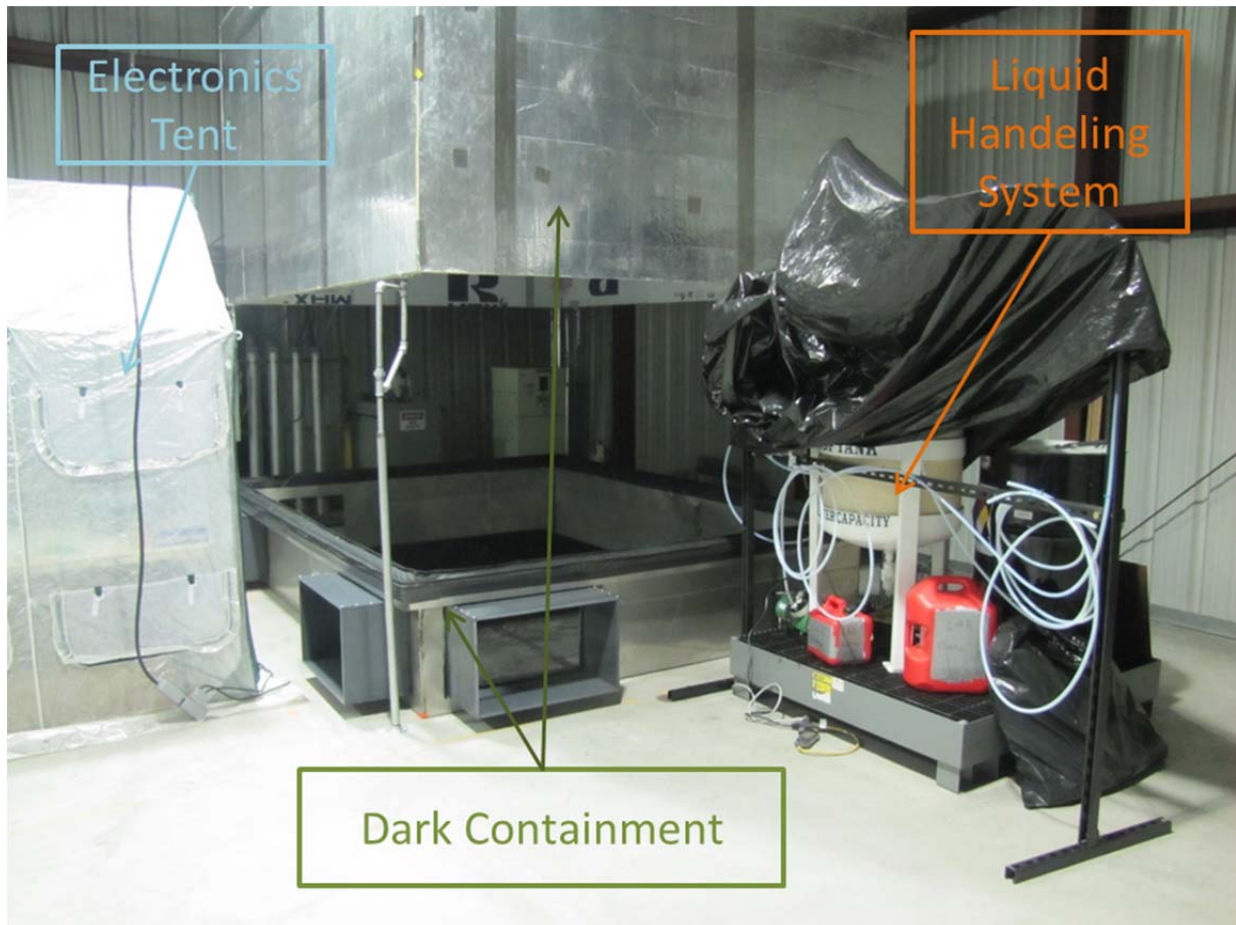Figure 15. Photograph of the stainless steel base for the Dark Containment.

Figure 16. The dark box built for the detector prototype, the tent with electronics, and the liquid scintillator filling system.

CHAPTER 6. MEASUREMENTS WITH THE μLENS DETECTOR

6.1. PMT characterization

We performed a series of measurements with the μLENS detector using PMTs in a variety of configurations placed on the surface of the detector. In order to make a clear way to identify the PMT locations we define a coordinate system to locate each cell and PMT. The center position of each cell and the locations of PMTs on the faces of the detector is an integer coordinate in each direction. The y-axis is the vertical direction and the x and z axes are in the horizontal plane. We enumerated the lattice positions by cell number from 1 to 6 with coordinates (i,j,k). The PMTs were mounted flush on the surface of μLENS to be easily moved and rearranged. The PMT positions are denoted by one of the 3 coordinates being either 0 or 7 corresponding to positions outside the lattice.

Four springs were attached to a collar fabricated from PVC that held the PMTs flush against the surface of the prototype, but allowed the PMTs to be easily rearranged on LENS. Before mounting the PMTs we first performed tests to characterize their relative gain and set approximate operating voltages. This consisted of two activities: a relative gain determination using the Compton edge as observed with a ^{137}Cs source and plastic scintillator, and characterization of the single photon response.

The relative gain of each PMT was tested by first setting the PMT up individually in a small dark box as illustrated in Figure 17. The PMTs viewed a block of plastic scintillator in a simple geometry and the scintillator was illuminated by a ^{137}Cs source. The voltage for each PMT was adjusted in order to set the 662 keV Compton edge, which is approximately 480 keV, to be at the same channel in the data acquisition. The location of the ^{137}Cs Compton edge in channels was recorded and fit vs. bias voltage to set relative gains of the PMTs. The PMT gains

were found to vary considerably, and a few were found to have such low gains as to have unsatisfactory performance even at the highest recommended bias voltages. These PMTs were rejected for use in μLENS.

The detector prototype with the PMTs mounted on the top is shown in Figure 18.

Figure 17. The miniature dark box for testing PMT gains.

Figure 18. The detector with the PMTs mounted on its surface.

We also conducted measurements to understand the single photoelectron response of the PMTs. Measurements were first conducted using 50 mm EMI model 9945B PMTs, which have documented single-electron response to validate our approach. The configuration used for these measurements is shown in Figure 19, where 2 of the EMI PMTS were setup to view a cylindrical

piece of plastic scintillator. One PMT, the "near PMT" was held at a fixed distance of 152 mm

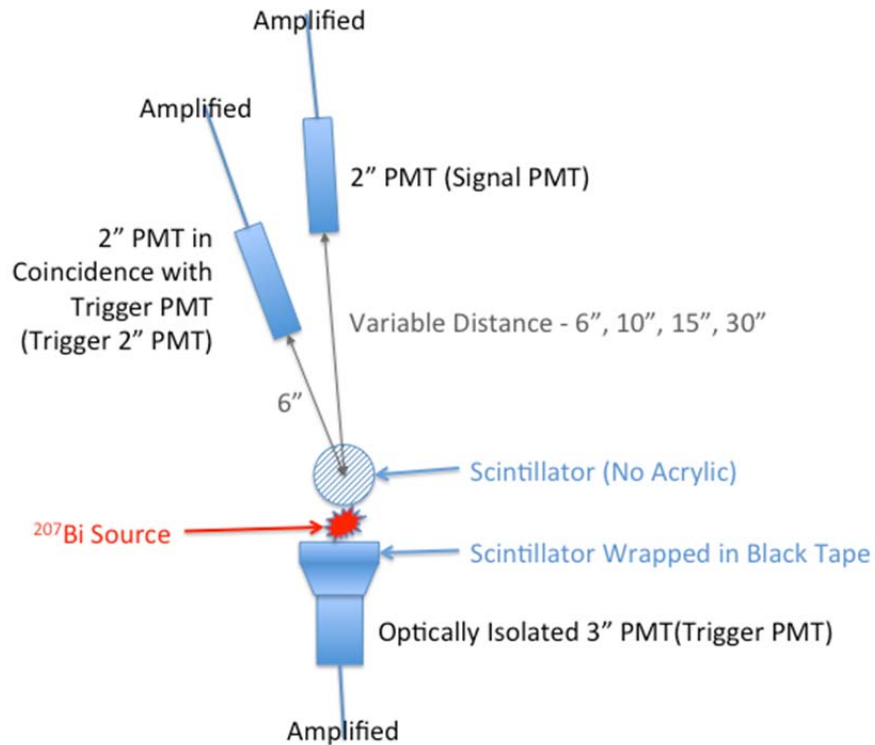(6 inches) to the scintillator, while the "single PE" PMT was placed at different distances.

Figure 19. The experimental setup used to study the single photoelectron response of PMTs.

A third 76 mm PMT, the "trigger PMT," was also coupled to a second piece of plastic

scintillator and optically segmented from the rest of the setup. A ^{207}Bi source, whose decay

spectrum is predominantly two gamma rays, a 1070 keV gamma ray and 570 keV gamma ray in

cascade, was sandwiched between the two optically isolated scintillators, one connetected to the

trigger and the other in the air and used to generate single photons detected at the far PMT.

Data collection was triggered in this setup by a hardware coincidence between the

optically isolated trigger PMT and the near PMT. A high hardware threshold was set on the

trigger PMT, while a low threshold was set on the near PMT. This provided a correlated signal

that removed most background events and achieved high selectivity for events resulting from

Compton scattering of the 570 keV gamma ray in one scintillator and the 1070 keV gamma ray in the other scintillator. An external amplification of 10 times was applied to all PMT signals. Waveforms were digitized (at 500 MHz) for both the near PMT and the "single PE" PMT. Codes developed for the μLENS DAQ were used to analyze each of the waveforms. Another reason for applying this approach to analyzing the waveforms is that it is similar to one we are currently exploring for performing an in-situ single photoelectron calibration of the μLENS PMTS.

Initially the PMT was placed at the same distance to the scintillator as the near PMT and a fixed time window was defined over which the voltage was integrated. We evaluated the waveform of the signal PMT by integrating the voltage over this fixed time interval. Measurements were then taken at increasing distances between the scintillator and the PMT being evaluated. There was little change in the shape of the spectrum in the "single PE" PMT observed between distances of 0.38 m (15 inches) and 0.76 m (30 inches), except for an increase in the fraction of counts in the zero peak. This is evidence that the spectrum is dominated by single photoelectron signals. A spectrum taken at a distance of 30 inches is shown in Figure 20. Since 30 inches was as great a distance as we could easily test in the dark-box being used, we further limited the incident light by masking the front of the PMT to effectively reduce the solid angle subtended by the PMT to a factor of 5 less than it subtended at a distance of 30 inches when unmasked. No change was observed in the spectrum other than the increase in the relative intensity of the zero peak, providing further evidence that the spectrum represents the single electron response. Comparison with other data shows that the shape of the spectrum is similar to expectations for the single electron response [48].

The single photoelectron response was also used to determine the gain of the PMT. This is derived by relating the current at the anode, $i_{anode}(t)$ of the PMT to the voltage read at the
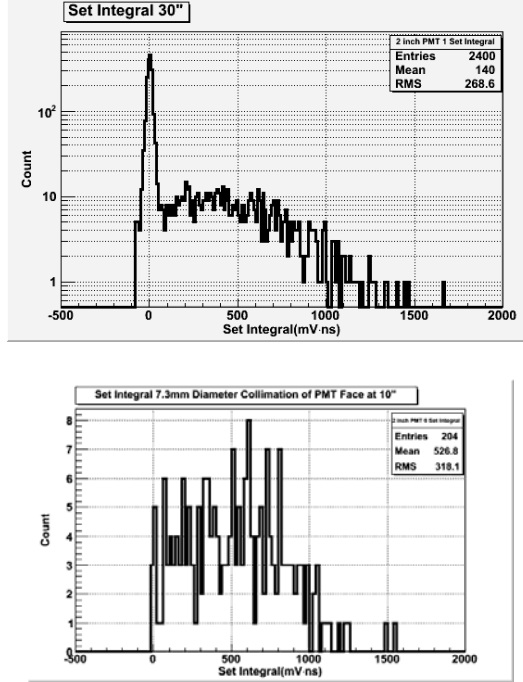
34

Figure 20a (top) and 20b (bottom). Integrated spectra for two different setups, an open face PMT at 30" from the scintillator (a) and at 10" with a cover on the PMT with a ~7.3mm diameter hole (b). Note that the zero peak has been subtracted in Figure 20b.

anode $V_{anode}(t)$,

$$i_{anode}(t) = \frac{dQ_{anode}(t)}{dt} = V_{anode}(t)/R$$

(7)

which can be rearranged to get the total amount of charge generated at the anode of the PMT as:

$$Q_{anode} = \frac{1}{R} \int V_{anode}(t)\,dt$$

(8)

The mean value of the integral for the single electron response is 500 mV•ns. With the R=50 Ω terminal resistance of the digitizer, we get a mean accumulated charge of 10 pC. But the digitized signal includes a 10x amplification external to the PMT, so the charge at the PMT anode is 1 pC, implying a gain for the PMT of 6×10^6. This is in line with the manufacturers' specifications for the EMI 9954B PMT of 5×10^6 at our operating voltage.

This same single photon analysis procedure was applied to a few selected Photonis XP3330 PMTs, the PMTs used in μLENS. In these measurements we also masked the XP3330 tube to reduce the solid angle so that the spectrum would be dominated by single photoelectron signals. A sample spectrum for a Photonis XP3330 PMT is shown in Figure 21. While we observed no difference in the shape of the collimated and uncollimated spectrum for the smaller EMI tubes, it may be questioned as to whether the resolution observed with an uncollimated XP3330 (which has larger area) would remain as good.
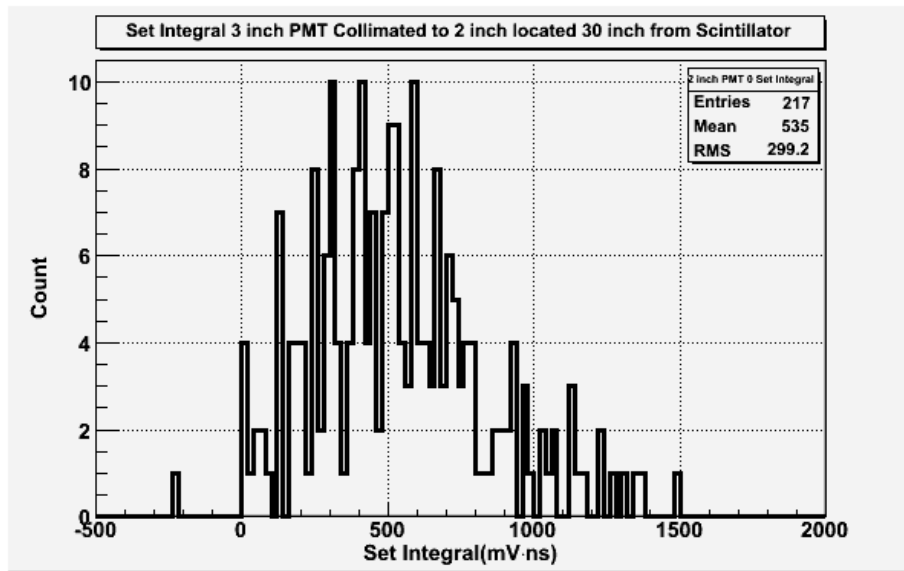

Figure 21. Sample single electron response for the Photonis XP3330. Note the expected (and measured) gains of the XP3330 at this operating voltage is the same as that for the EMI 9954B described above.

6.2. Light propagation with the μLENS

One of the main goals with the μLENS detector is to study light propagation in the lattice architecture. Data were collected using a simplified data acquisition system (DAQ) based on the CAEN Versa Module Europa (VME) Model 792 Charge-to-Digital converters (QDCs) and Model 775 Time-to-Digital converters (TDCs). This simplified DAQ allows studies with μLENS to go forward while the multiplexed DAQ based on transient digitizers is developed for

miniLENS in parallel. The initial μLENS program was limited to 96 channels by the availability of QDCs. This somewhat restricts the variety of measurements, though not much beyond our restriction of 110 working PMTs. However, we have developed a targeted program of measurements that addresses the main issues of light channeling and attenuation in the lattice.

Because the light from a scintillator is generated along the track of the ionizing particle, it is possible to determine the position of interaction by localizing the source of the scintillation light. Due to the total internal reflection, two opposite PMTs on μLENS can be treated similarly to two PMTs positioned at either end of a long bar of scintillation material. In this type of geometry, the intensity of the light measured at one end of the rod drops off exponentially with the distance at which the scintillation light is generated. Thus, we can write for the signal from one PMT [48]:

$$E_1 = \frac{E_\gamma P}{E_0} exp\left[-\alpha\left(\frac{L}{2} + x\right)\right] \qquad (9)$$

where E_γ= energy deposited by a gamma ray, P= probability that the light quantum produced will hit one end and generate a photoelectron in adjacent PMT, E_0= energy deposited per light photon created in scintillator, α= light attenuation coefficient, L=distance between the two PMTs (length of the scintillator bar), x=position of the energy deposit in the scintillator. Similarly, for the second PMT:

$$E_2 = \frac{E_\gamma P}{E_0} exp\left[-\alpha\left(\frac{L}{2} - x\right)\right] \qquad (10)$$

By dividing the signal in one PMT by the other, we obtain:

$$\frac{E_2}{E_1} = \frac{exp\left[-\alpha\left(\frac{L}{2}-x\right)\right]}{exp\left[-\alpha\left(\frac{L}{2}+x\right)\right]} = exp(+2\alpha x) \qquad (11)$$

$$\ln\left(\frac{E_1}{E_2}\right) = 2\alpha x \qquad (12)$$

$$x = \frac{1}{2\alpha} ln \frac{E_2}{E_1} \qquad\qquad\qquad (13)$$

Therefore, by determining the logarithm of the ratio of the two PMT signals, we obtain a linear indication of the position where the scintillation occurs. By multiplying (9) and (10), we obtain:

$$E_\gamma^2 = E_1 E_2 \left(\frac{E_0}{P}\right)^2 e^{\alpha L/2} \qquad\qquad (14)$$

Thus, the square root of the product of the two PMT signals serves as a measure of the total scintillation light, independent of the position within the bar, or within μLENS. It should be noted that when applied to μLENS, the parameter α is not a true attenuation coefficient, but represents loss of light that is not channeled by TIR down the main axis.

An alternative method of sensing the scintillation position in one dimension is to use the same geometry described above but to exploit the fact that there will be a slight difference in the time of arrival of the scintillation light at the two ends of the bar. This time difference is maximum for an event that occurs at either end of the bar and decreases to zero for an event at the center. The time differences are small, since the velocity of propagation of the light traveling directly from the scintillation site is c/n, where c is the velocity of light and n is the index of refraction of the scintillation medium. Furthermore, given the significant attenuation of light with position, we expect charge division to give a better determination of the position in μLENS.

Using this principle with the μLENS prototype, we performed a number of measurements of how light propagates in the μLENS lattice. The lattice architecture of μLENS allows the origin of the light to be determined independently from the signals from two trigger PMTs placed opposite to each other on the faces of the detector prototype. We define the position of the event from PMTs sitting in the same plane but perpendicular to the trigger PMTs in the same way as we did with the trigger PMTs, thus cross-checking the position of the event. Then we

compare the position of the event to those determined from the trigger PMTs and calculate the attenuation coefficient α. Our analysis is also guided by Monte Carlo simulations, which indicate that the fraction of light collected by a PMT has a complicated dependence on the distance from the point of origin in μLENS. Due to the small scale of the instrument, the dominant factor is the lattice geometry, but there is also substantial attenuation owing to the relatively thick Teflon film, with a small attenuation length, used in the μLENS prototype, and the reflections on the air-acrylic boundaries at the edge of the μLENS detector. Despite these complicated dependences, the sum of the QDC output of opposite facing PMTs provides a measure of the energy deposited that is minimally dependent on the location of the event or the degree of attenuation for signals that are not close to the edges of the detector. We tested our understanding of light propagation in the instrument by comparing the results from measurements with an external source to Monte Carlo simulations.

The difference between the amount of light observed in opposite PMTs is indicative of the position of energy deposition within the detector, just as in a long bar of scintillator. It is illustrative to model the fraction of light detected as having an exponential dependence on distance to the PMT, while keeping in mind that the actual μLENS lattice dependence is more involved.

If the fraction of light observed has an exponential dependence on distance, the total energy deposited is proportional to the geometric mean of the light observed of any two facing PMT. A comparison of the arithmetic mean $(E_1 + E_2)$ and the geometric mean $\sqrt{E_1 * E_2}$ is shown in Figure 22. The total energy calculated using the arithmetic and geometric means agree well with each other. These two methods can be related via simple expansions of Equation (10) and Equation (11). The general agreement means that the leading term in the exponential
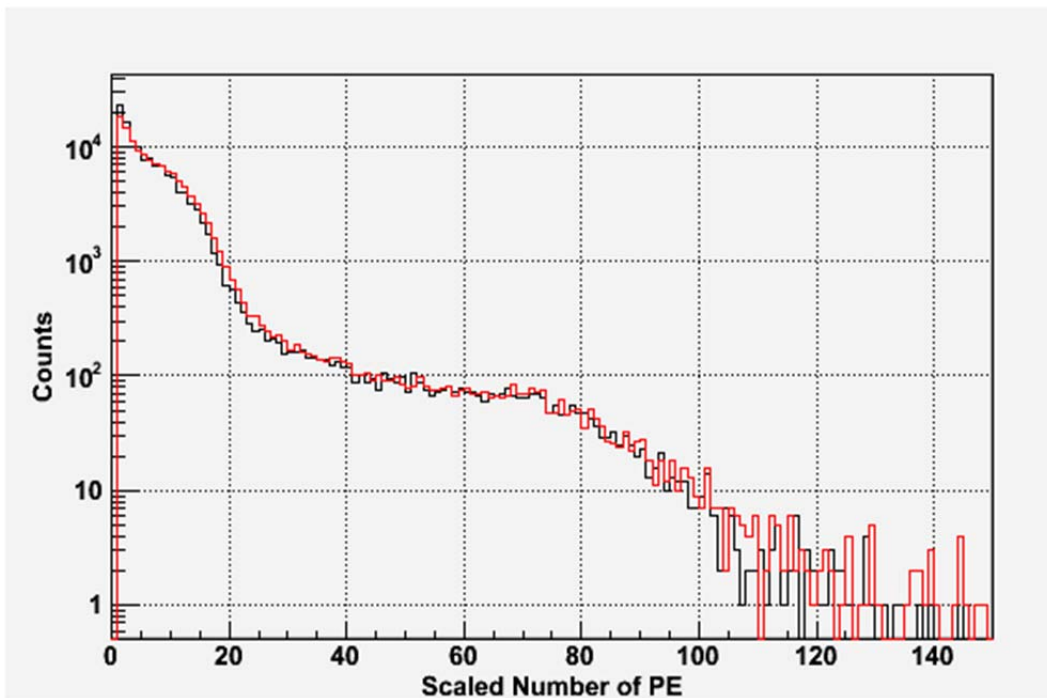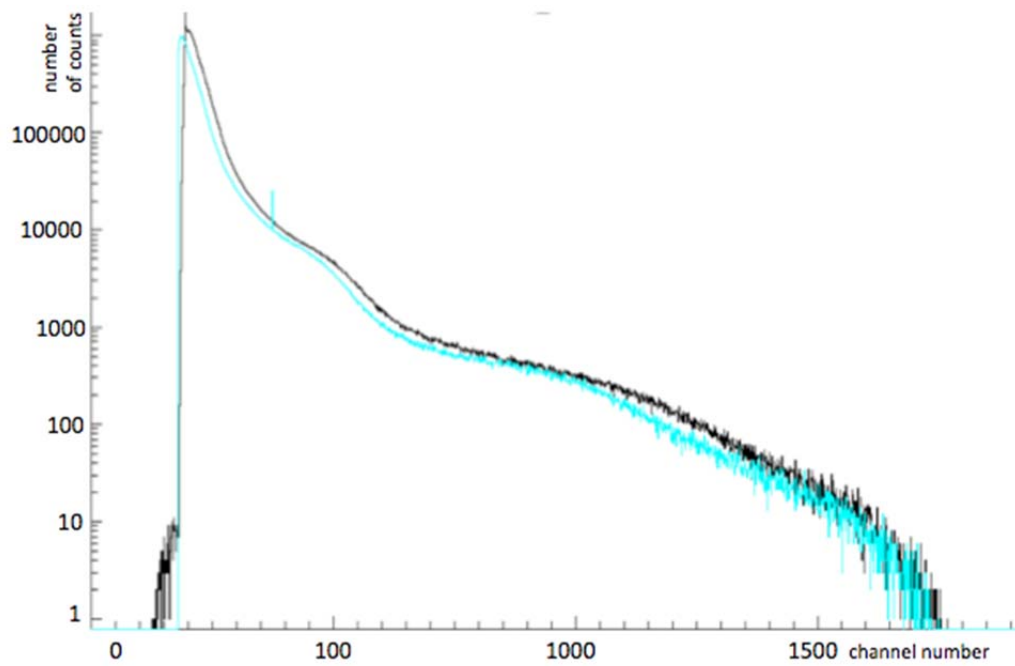
Figure 22, (top) Measured comparison of geometric and arithmetic mean of facing PMT using
^{137}Cs source. The higher energy is due to background. (bottom) Simulated comparison of
geometric and arithmetic mean of facing PMT using ^{137}Cs source. The Compton edge is around
channel 70.

expansion dominates using the sum $E_1 + E_2$ will lead to computationally faster real time analysis for LENS since the square root function is computationally expensive.

While the difference in the signal observed by the opposite PMTs provides a measure of the position of energy deposition, the LENS architecture also pinpoints the origin of light by channeling along the planes of the scintillation lattice. Correlating position using these two techniques provides insight into light propagation and attenuation in the lattice. Figure 23 shows the measured and simulated difference of the QDC output for two opposite PMTs with the additional cut on the maximum sum of paired facing perpendicular PMT QDC output. There are distinct peaks with a shift when gating on position from the opposite face that is in qualitative agreement with predictions of the Monte Carlo model.
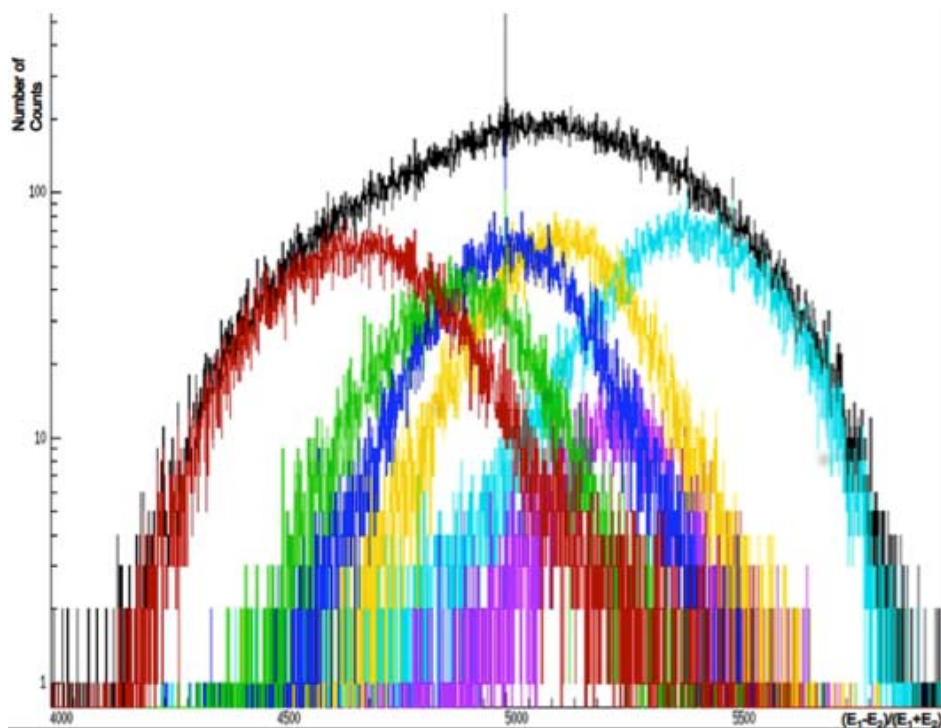

Figure 23. Measured (top, a) difference of facing PMT QDC output of a ^{137}Cs source outside of micro-LENS.
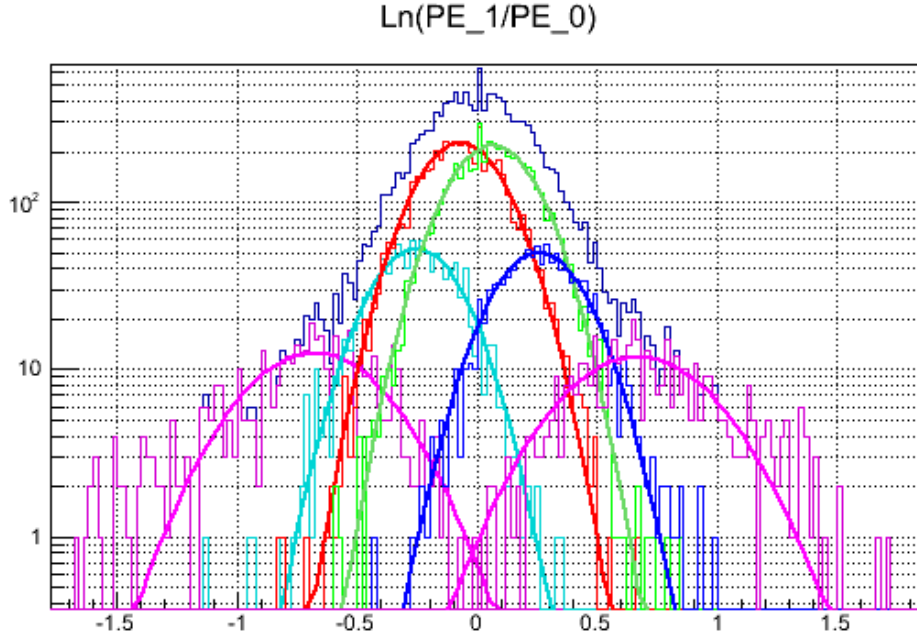
41

Figure 23, continued. Simulated (bottom, b) difference of facing PMT QDC output of a ^{137}Cs source outside of micro-LENS.

The relative counts and widths in the measured data are affected by background, poor PMT gain matching, and that gamma rays deposit energy in multiple cells make the peaks broader than they would be with an electron source.

In the approximation that the light observed by a PMT has an exponential dependence on position, the position of the event is linearly related to the natural log of the ratio of the signals by $x = \frac{\ln\left(\frac{E_1}{E_2}\right)}{2a}$. We take the difference of light seen by the opposite PMTs and divide it by the sum of light seen by the opposite PMTs. The parameter α is similar to an effective attenuation, but this is also influenced by geometric effects due to the small size of μLENS. If we exclude light originating in the outer layer of cells, this effect is largely minimized. The measured and simulated plot of the natural log of PMT centroids is shown in Figure 24. We perform a linear fit and calculate α, since the slope should be 2α. We only fit the inner 4 cells of the detector, due to the excess light detected from events in the outer cells. From the simulations in Figure 24, we

calculate an α of 0.082 ± 0.001 per cell. From the peak positions of the various PMT Q measurements we calculate the α to be 0.0116 ± 0.004 per cell. The attenuation of light that we measure in the lattice is greater than that predicted with an ideal model of the detector in the simulations, *i.e.* there were no imperfections modeled in the lattice.
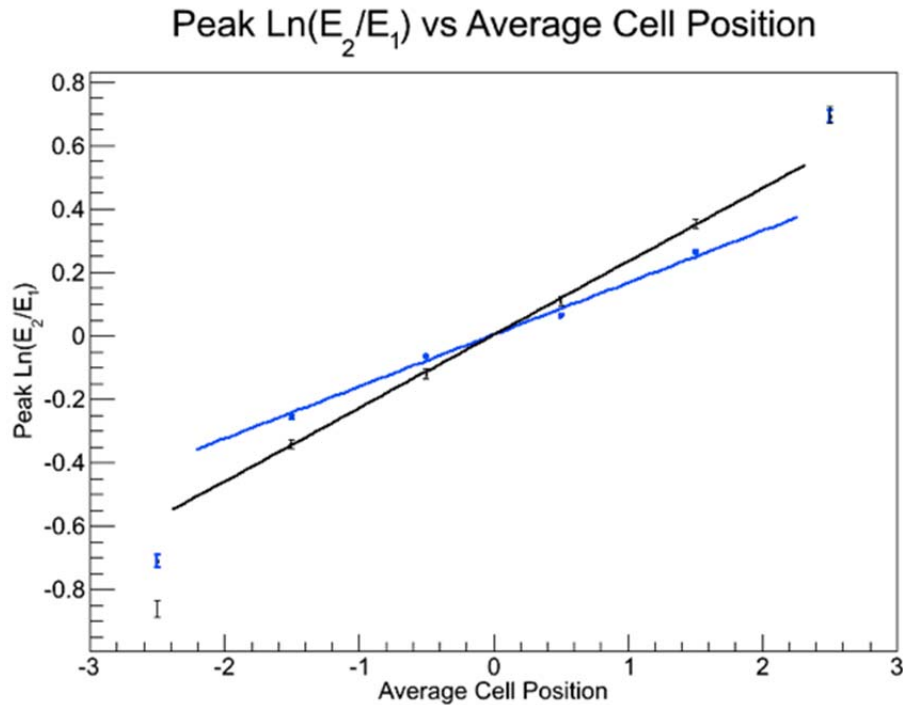

Figure 24. Measured (black) and simulated (blue) linear fit of PMT positions different distance from the event extracted from centroid distributions. The attenuation coefficient α is determined from a linear fit to the data from the central 4 cells.

Another type of measurement tests how light channels out of μLENS. Due to the relative indices of refraction of teflon and the LAB scintillator not all of the light should channel directly out of μLENS, but in fact should spray in a more complicated manner as shown in Figure 25. Due to the values of the indices of refraction of the Teflon lattice and the scintillator 65% of light gets channeled into the main PMTs of the detector. The rest is sprayed in the plane of the detector, in which the light was deposited. If we simulate this effect, we find 69% of
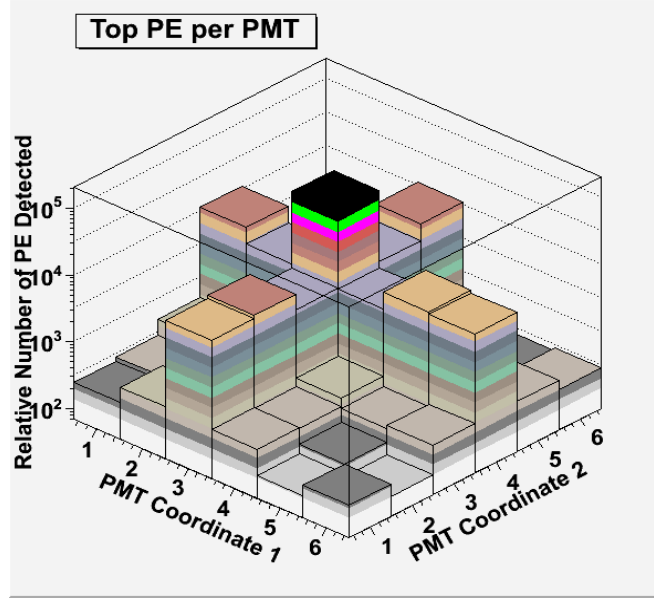
Figure 25. Simulation of the number of PE detected for the top face of miniLENS for a 511 keV electron in a cell near the center of the detector. Sum of main channel to single plane is ~65%. Prediction of single lattice element ~69%.

light is channeled, in good agreement with simulations. In another set of measurements we studied the light propagation within planes inside the detector. Trigger PMTs were arranged on the top of the detector, in positions (3,7,3), (3,7,4), (4,7,3), (4,7,4) near its center, and a radioactive source (^{137}Cs) of approximately 0.5 μCi was placed underneath, also near the center of the detector. Signal PMTs were arranged on horizontal planes covering all side faces, especially (i,2,k), (i,3,k), (i,4,k), and (i,5,k), where i, k=1-6, as shown in Figure 26. Interpretation of data from the top and bottom planes is more complicated due to the edge effects from scattering from the air boundary on the sides of the detector.

Data from planes Y=2 are shown in Figure 26. Events with the PMT setup shown in Fig 26 can be divided into three general categories: (1) the signals in the trigger PMTs are small and the energy deposited in the plane is large, (2) the trigger signal is proportional to the light deposit in the plane, and (3) there is a large signal in a trigger PMT and little energy deposited in the plane. The small trigger signal and large plane sum of the deposited light (1) happen when most
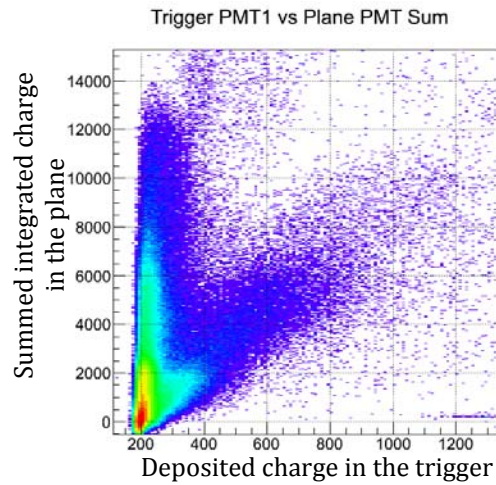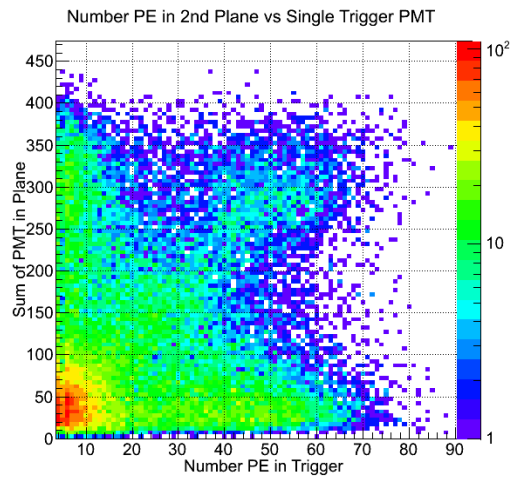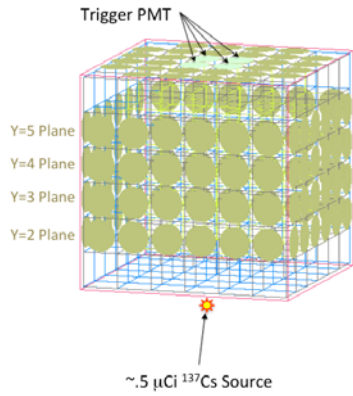
Figure 26. The detector setup prototype (top) with a ~.5 μCi ^{137}Cs source located near the center in bottom of μLENS, and the Geant4 simulations prototype (middle) of the detector with the ^{137}Cs source. Data taken with the detector (bottom). The light is seen by the trigger PMTs in the y=2 plane. Only two of the three regions are seen since the trigger associated with this particular deposition in the trigger cell was not working.

of the energy is deposited outside of the column that the trigger PMT views on top of the detector. The small plane sum and large trigger (2) occurs when there is a large energy PMT column but the vertex lies outside of the Y=2 plane. The proportional area of the histogram (3) occurs when most of the energy deposit is in the center of the Y=2 plane. We find at least quantitative agreement between measurements and our expectations from simulations. It turned out that that one of the triggers was not performing correctly, and we only collected the light seen by the other PMT triggers in the Y=2 plane. The data from the entire second (Y=2) plane of the μLENS were compared to the computer simulations performed in Geant4 (Figure 26).

6.3. LED tests

To understand the propagation of light within the lattice and to calibrate the response of the PMTs, it is desirable to inject a well-understood optical signal into μLENS. Various techniques can be used to create fast optical pulses. For μLENS a highly directional monochromatic beam of light is advantageous to test the robustness of the lattice construction. The simplest method of creating well-defined optical pulses in the required nanosecond range involves the use of lasers. Lasers of a semiconductor nature are also beneficial at the required frequency of operation because they can be controlled by simple modulation of the biasing current. A disadvantage carried by the laser technology is that the laser setups are expensive. An alternative to laser technology is the use of Light Emitting Diodes (LEDs), which have the advantages of reduced cost and they produce isotropic radiation. Development of low cost, high speed LEDs has made these devices suitable for use as pulsed light sources of the kind required for the proposed PMT calibration and to test the μLENS lattice. The emitted optical spectrum of these devices has been considerably extended into the blue end of the spectrum in recent years, allowing good spectral match of the emitted light with the light that the PMTs are most sensitive.

46

These devices are currently capable of radiating from the Ultraviolet (UV) to the Infrared (IR) section of the spectrum.

In order to better understand the μLENS performance and light channeling in the detector (see Figure 27 for a picture of light channelling), we have tested the μLENS with a setup of collimated pulsed LEDs.
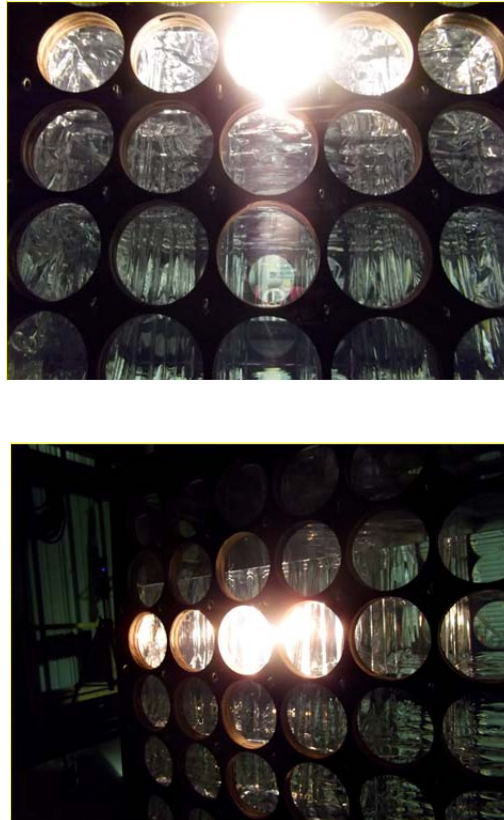

Figure 27. Shining a flashlight into one side of μLENS. We have redone this experiment quantitatively and measured the amount of light collected by each PMT using collimated LEDs. The pulses were generated by the pulse generator, which powered one LED at a time. We were trying to estimate light collection in each PMT opposite to the shining LED, as well as estimate the amount of light leaked into cells that were not directly opposite to the shining LED.

A total of 32 blue Surface-Mount Device (SMD) LEDs (Figure 28) were instrumented on a board to match the lattice of the detector and then connected to a Model HP 81110A pulse generator through a ribbon cable. Photonis XP 330 PMTs were instrumented on the top of the

Figure 28. LED setup. The collimated LEDs are being switched on, and light is collected by a PMT.

µLENS detector. For every run the voltage on the pulse generator was set to 7 V, and the length of the pulse was 14-30ns. Each Photonis PMT HV was set at 1200 V. The data from runs were recorded by a data acquisition system. LEDs were collimated (Figure 28) so that all of the light entering the prototype should be at angles such that all the light is totally internally reflected to the opposite face. This model is confirmed by Geant4 simulations (Figure 29).

We flash one LED and look at the pattern of light collected by the opposite PMT. We expected that all the light flashed by the LED would be channeled across the prototype and collected by the opposite PMT, but in fact there was significant (12%) leakage of light into the cells adjacent to the one opposite the LED, see Figure 29 (top). We tried to solve this puzzle by putting a PMT opposite each of the LEDs, see Figure 28, and flashing them one at a time.

With this arrangement we expect light only when one LED (one opposite the PMT) is flashed. However, we found significant light in the PMT when neighboring LEDs were flashed indicating that the LED light is reflected from the walls of the collimating tube surrounding the LED since the tube is not black, and enters a cell in the detector prototype under the angle less than the angle of total internal reflection angle, which prevents it from totally internally reflecting back into the cell.

As a result, the light is not created, and hence not channeled, in the way we expect. A significant amount of light is lost into the neighboring channels. The fraction of non-channeled light was found to be in good agreement with the amount of light reflected from the collimators. We are now improving the LED tests with better collimators.
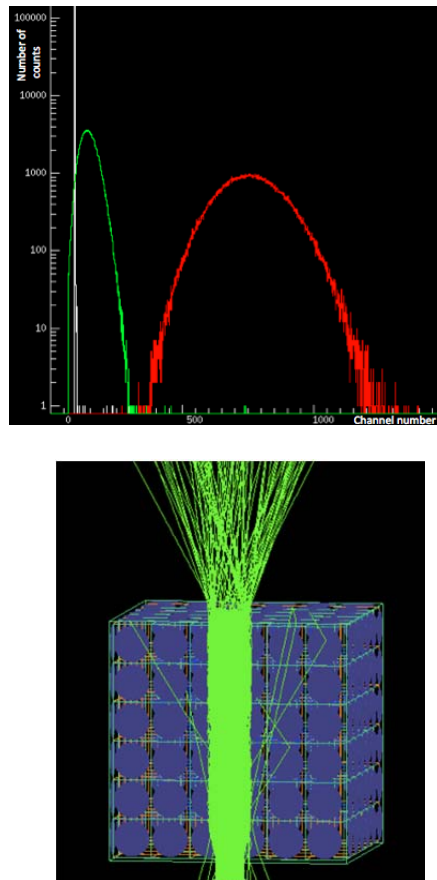

Figure 29. The LED light collected. Top: the red spectrum represents light collected by a PMT in a cell opposite the LED, and the green spectrum represents light from a cell neighbouring to the one with the LED. Bottom: the detector prototype simulations.

49

CHAPTER 7. FUTURE RESEARCH PLANS: MINILENS

The μLENS detector prototype is the first step towards demonstrating the capabilities of LENS. It has been operating underground at KURF since late 2011 with no shielding and PMTs mounted flush on the face of the instrument. While the primary experimental goal of testing light transport in the as-built lattice does not require operation underground, deployment of the μLENS at KURF has been crucial in developing equipment and on-site techniques towards the miniLENS prototype. MiniLENS is the next stage in the development of the future LENS detector. With miniLENS we will demonstrate the full sensitivity required for a precision measurement of the lowest energy solar neutrinos. We will also test scintillator handling, which will be indium-loaded this time, a new data acquisition system using multiplexed PMTs, and shielding against external background. We anticipate an exquisitely sensitive detector capable of examining the whole range of parameters needed for LENS (and indeed for other applications of the novel 'optical lattice' design).

Many of the components for the miniLENS design have largely been tested and refined with the construction of μLENS. The lattice for miniLENS will use similar construction techniques and similar fluid handling systems. However, the sides of the lattice, and light guides to transport light through the water shielding are new and designed to minimize material (and thus radioactivity). The primary difference with miniLENS is that we aim for background levels comparable to neutrino events. The components for miniLENS are now being fabricated.

We can complete construction of the 410-liter miniLENS prototype using 162 PMTs (sufficient to implement 2 faces of the detector). Alternate configurations, however, can reveal complementary information, such as self-shielding of the scintillator. Thus, we built in the ability to rearrange PMT coverage. Instead of 2 full faces, we could also instrument only the

central 7x7 positions on 3 faces and/or the central 5x5 positions on all six faces. By combining these three types of measurements, we can perform the kind of indirect characterization as described previously. However, such a series of studies with fractional PMT coverage (and resulting sub-optimum energy resolution) will not allow us to achieve the direct and absolute measurement of the background level that instrumenting the water shield allows. Therefore, there is a proposal to upgrade miniLENS to double the PMT coverage and add the necessary channels of electronics.

A large reduction in external background is required to reach the target background levels for miniLENS, and a water shield of about 2 m in thickness is required. A passive water shield has a clear advantage in that there is substantial previous experience and high radiopurity is possible. Scintillator also has advantages (e.g. favorable index of refraction), but we have opted to implement water in the initial phase due to its relative simplicity, low cost, and low risk. The external background will be reduced by attenuation in the water shielding and by cuts within the detector. To efficiently estimate the shielding requirements, we have performed Monte Carlo simulations with miniLENS with no external passive shield to study the effectiveness of the internal cuts. There are several important background signals that warrant individual mention. The 0.6 MeV ^{214}Bi line is particularly dangerous due to the close proximity of its energy to the total gamma-ray cascade energy of interest. However, external ^{214}Bi is heavily suppressed by the water shielding due to the low energy of the gamma ray. The primary danger from this decay arises from internal sources of background, and relatively stringent requirements for U radiopurity are required for the internal components. For the higher energy gamma ray lines, a 2 m water shield reduces their background to a fraction of an event/year, and the total expected background is comparable to that from the pp neutrino flux (2/yr in the miniLENS fiducial

51

volume). With these calculations as a basis, we have chosen to implement the largest possible water shield that can be constructed off site and delivered assembled, which will provide more than 2 m water shielding. More detailed simulations are now ongoing to study factors like neutron production in the water shield and cosmogenesis, which thus far have not been included.

MiniLENS requires light guides to transport the channeled light from the lattice through the water to the PMTs mounted outside of the water tank. While it is common to use acrylic light guides the radio-purity requirements and cost disfavor this method. We believe that we can build guides made from clear and reflective films that incorporate an air-gap for efficient light transport. Since this is a novel technique careful simulation, benchmarking, and testing are required in order for the guides to be successfully incorporated into the miniLENS design. We have are working on an apparatus to test the light guides while submerged in water to better judge their performance in an as built miniLENS. We have developed a simple and flexible means of testing prototype guides in the lab. We have tested the water tightness of the apparatus, but more work is needed including the addition of fill and drain ports as well as the construction of a holding mount in the dark box.

For CNO neutrinos, the implementation of the water shield allows the basic function of the LENS design to be demonstrated readily with miniLENS. However, for the pp neutrinos the task is more complicated. The intrinsic In background can create 'false tags' primarily through single decays (type A), two decays in (10 ns) coincidence (type B), or three decays in coincidence (type C). As shown in Table 1, type B is the most challenging, requiring 'topology' cuts. Since the rates in miniLENS are very low, one can open up the coincidence window between two In decays and greatly increase the rate of these 'false tags' to accurately characterize this background and the effectiveness of cuts in reducing them. This increase is

even greater for type C backgrounds. However, type A backgrounds are 'singles' events, and their rates cannot be artificially increased this way, and thus they set the scale for shielding and length of runs. MiniLENS can be run with the PMTs directly against the detector, with and without In loading in the scintillator, and then again with the PMTs outside the water shield (using light guides) again in principle with an In-loaded scintillator.

The nearing completion of miniLENS as a testing facility for the LENS experiment ushers in a productive period ahead for the LENS collaboration. With the modest upgrades described above, we anticipate an exquisitely sensitive detector capable of examining the whole range of parameters needed for LENS and for other applications of the novel 'optical lattice' design.

REFERENCES

[1] J. N. Bahcall, M. N. Pinsonneault, Neutrino 96, Proceedings of the 17 International Conference on Neutrino Physics and Astrophysics (1996).

[2] J. N. Bahcall, arXiv: physics, 0411190v (2004).

[3] R. d'E Atkinson, Astrophysical Journal 84, 73 (1936).

[4] C. Iliadis, Nuclear Physics of Stars, betz-druck GmbH, Darmstadt: John Wiley & Sons (2008).

[5] F. Fang, The University of Michigan Ph.D. Thesis (2012).

[6] E.G. Adelberger et al., Reviews of Modern Physics 83, 195 arXiv:1004.2318 (2011).

[7] R. Davis et al., Physics Today 17 (1990).

[8] The GALLEX team, Physics Letters B 285, 376 and 390 (1987).

[9] J. N. Bahcall and H. A. Bethe, Physical Review D 47, 1298 (1993).

[10] J.N. Bahcall et al., preprint IASSNS-94/13 received at the National Radio Astronomy Observatory (1994).

[11] J. N. Bahcall and A. M. Serenelli, Astrophysical Journal 621:L85-L88 (2005).

[12] A. Suzuki in M. Fukugita (ed.), A. Suzuki (ed.): Physics and astrophysics of neutrinos, 388-447, (1994).

[13] Y. Fukuda et al., Physical Review Letters 81, 1562 (1998).

[14] B. Pontecorvo, Journal of Experimental and Theoretical Physics 33, 549–551, (1957), reproduced and translated in Soviet Physics Journal of Experimental and Theoretical Physics 6, 429 (1957).

[15] B. Pontecorvo, Journal of Experimental and Theoretical Physics 53: 1717 (1967), reproduced and translated in Soviet Physics Journal of Experimental and Theoretical Physics 26, 984 (1968).

[16] M. Nakahata et al., Nuclear Instruments and Methods in Physics Research A421, 113 (1999).

[17] S. M. Oser in Y. Suzuki (ed.) The Third International Workshop on Neutrino Oscillations and Their Origin: Tokyo, Japan, 5-8 December (2001).

[18] F. Beacom and P. Vogel, hep-ph/9903554, Physical Review Letters 83, 5222 (1999).

[19] Q. R. Ahmad et al., Physical Review Letters 87 (7), 071301 (2001).

[20] A.W.P. Poon et al., Nuclear Instruments and Methods in Physics Research A452, 115, (2000).

[21] S. Fukuda et al., Physical Review Letters 86, 5651 (2001).

[22] G. L. Fogli, E. Lisi, A. Palazzo and F. L. Villante, Physical Review D 63, 113016 (2001).

[23] Borexino Collaboration, Nuclear Instruments and Methods in Physics Research A 600, 568 (2008).

[24] C. Arpesella et al., Physics Letters B 658, no. 4, 101-108 (2008).

[25] G. Bellini et al., Physical Review D 82, 033006 (2010).

[26] G. Bellini et al., Physical Review Letters, 108 (2012).

[27] G. Bellini et al., Physical Review Letters, 107, 141302 (2011).

[28] K. Nakamura and Particle Data Group, Journal of Physics G: Nuclear and Particle Physics 37, no. 7A 075021 (2010).

[29] G. Bellini et al., Physics Letters B 707, no. 1 22 – 26 (2011).

[30] G. Bellini et al., Physics Letters B 687, 299 (2010).

[31] J. N. Bahcall, Physical Review C 65, 025801 (2002).

[32] R. S. Raghavan, Physical Review Letters 37, 259-262 (1976).

[33] G. Audi, et al., Nuclear Physics A 729, 337 (2003).

[34] F. P. An et al., Physical Review Letters 108, 171803 (2012).

[35] J. K. Ahn et al., Physical Review Letters 108, 191802 (2012).

[36] V. Barger, P. Huber and D. Marfatia, Physical Review Letters 95, 211802 (2005).

[37] M. Cirelli, M. C. Gonzalez-Garcia and C. Pena-Garay, Nuclear Physics B 719, 219 (2005).

[38] R. Fardon, A. E. Nelson and N. Weiner, Journal of Cosmology and Astroparticle Physics 0410, 005 (2004).

[39] K. Eguchi, et al., Physical Review Letters 90, 021802 (2003).

[40] M. Asplund, N. Grevasse and A. Sauval, Proceedings of Astronomical Society of the Pacific Conference Series 336, 25 (2005).

[41] M. Asplund, N. Grevasse, A. Sauval and P. Scott, Annual Review of Astronomy and Astrophysics 47, 481 (2009).

[42] A. Gervais and A. Sauval, Space Science Review 85,161 (1998).

[43] A. M. Serenelli, W. C. Haxton and C. Pena-Garay, Astrophysical Journal 743, 24 (2011).

[44] W. Haxton and A. Serenelli, arxiv: 0805.2013 (2008).

[45] W. C. Haxton, R. G. H. Robertson and A. M. Serenelli, arxiv: 1208.5723 (2012).

[46] C. Kraus et al., Progress in Particle and Nuclear Physics 64, 273 (2010).

[47] R. Saldanha, Princeton Ph.D. Thesis (2012).

[48] G. F. Knoll, Radiation Detection and Measurement: Third Edition. Hoboken, NJ: John Wiley & Sons, (2000).

[49] J. N. Bahcall et al., Physics Letters B 433, 1 (1998).

[50] B. T. Cleveland et al., Nuclear Physics B (Proceedings Supplements) 38, 47 (1995).

[51] P. Anselnmann et al., Physics Letters B324, 440 (1995).

[52] J. N. Abdurashitov et al., Physics Letters B328, 234 (1994).

[53] B. K. Kim et al., Proceedings of the 26th International Cosmic Ray Conference, Salt Lake City (1999).

[54] S. P. Mikheyev & A.Y. Smirnov, Soviet Journal of Nuclear Physics 42, 913 (1985).

[55] Y. Koshio et al. in Y. Suzuki (ed.) The Third International Workshop on Neutrino Oscillations and Their Origin: Tokyo, Japan, 5-8 December (2001).

[56] M. B. Smy for the Super-Kamiokande Collaboration, Journal of Physics Conference series, 203: 012082, (2010).

[57] K. N. Abazajian, arXiv: 1204.5379, (2012).

[58] C. Grieb, J. M. Link and R. S. Raghavan, Physical Review D 75, 093006 (2007).

[59] J. N. Bahcall Neutrino Astrophysics, Cambridge University Press: First edition (1989).

VITA

Liudmyla Afanasieva, a native of Ukraine, got her Bachelor of Science degree from Kharkiv National University in 2009. Afterwards she made the decision to enter graduate school in the Department of Physics and Astronomy at Louisiana State University. She expects to receive her master's degree in May 2014 and plans to begin work on her doctorate upon graduation.